

Abstract

McCrain, Laura Lynne. The Effect of Elevated Pressure on Soot Formation in a Laminar Jet Diffusion Flame. Under the direction of Dr. William L. Roberts.

Soot volume fraction (f_{sv}) is measured quantitatively in a laminar diffusion flame at elevated pressures up to 25 atmospheres as a function of fuel type in order to gain a better understanding of the effects of pressure on the soot formation process. Methane and ethylene are used as fuels; methane is chosen since it is the simplest hydrocarbon while ethylene represents a larger hydrocarbon with a higher propensity to soot. Soot continues to be of interest because it is a sensitive indicator of the interactions between combustion chemistry and fluid mechanics and a known pollutant. To examine the effects of increased pressure on soot formation, Laser Induced Incandescence (LII) is used to obtain the desired temporally and spatially resolved, instantaneous f_{sv} measurements as the pressure is incrementally increased up to 25 atmospheres. The effects of pressure on the physical characteristics of the flame are also observed. A laser light extinction method that accounts for signal trapping and laser attenuation is used for calibration that results in quantitative results. The local peak f_{sv} is found to scale with pressure as $p^{1.2}$ for methane and $p^{1.7}$ for ethylene.

**THE EFFECT OF ELEVATED PRESSURE ON
SOOT FORMATION IN A LAMINAR JET
DIFFUSION FLAME**

by

Laura Lynne McCrain

A thesis submitted in partial fulfillment of the requirements for the degree
of Master of Science

Aerospace Engineering

North Carolina State University

2003

Approved by:

Dr. William L. Roberts
Chair of Supervisory Committee

Dr. Jack R. Edwards
Member of Supervisory Committee

Dr. Stefan Franzen
Member of Supervisory Committee

Biography

The author was born Laura Lynne McCrain on February 11, 1979 in Hendersonville, NC, the only child of Don and Sara McCrain. She graduated from North Henderson High School. Awarded a Park Scholarship, the author chose to attend North Carolina State University and major in aerospace engineering. Upon the completion of her undergraduate degree in May 2001, Laura decided to prolong her collegiate experience and pursue a Master of Science in aerospace engineering. During her first year of graduate school, she applied for and received a National Science Foundation Graduate Research Fellowship, which in some part influenced her in deciding to pursue a doctorate.

Acknowledgements

The author would like to acknowledge her advisor, Dr. William Roberts, whose ability to instruct and appreciation of knowledge are to be commended; Dr. Michele DeCroix, Dr. Eric Welle, Jidong Xiao, and Nicole Erickson for their advice and assistance; her parents, Don and Sara McCrain, for never questioning her abilities or goals and for emphasizing the importance of sensibility, hard work, and consideration; Dixie and Scout for making home something to look forward to at the end of the day; and finally, Will Barnwell for his unflagging support and commitment to our present life together and the life we both eagerly anticipate for the future.

Table of Contents

List of Figures	v
1 Introduction	1
1.1 Soot Formation.....	1
1.2 Effects of Elevated Pressure on Soot Formation	5
1.3 Laser Diagnostic Techniques.....	7
1.3.1 Laser Extinction.....	7
1.3.2 Laser Induced Incandescence.....	8
2 Experimental Apparatus and Conditions	10
2.1 Co-flow Diffusion Flame Burner	10
2.1.1 Burner Geometry	10
2.1.2 High Pressure Vessel	12
2.1.3 Ignition System	13
2.1.4 Flow and Pressure Control System	15
2.2 Physical Appearance of Flame	17
2.3 Laser Induced Incandescence	23
2.3.1 Optical Set-up	24
2.3.2 Timing and Wiring	26
2.4 Extinction Measurements	27
3 Extinction Measurements and Soot Volume Fraction.....	31
3.1 Extinction Measurements as Calibration.....	31
3.2 Soot Volume Fraction.....	31
4 Calibration of LII Measurements	36
4.1 Correction of Raw LII Signal	36
4.1.1 Background Noise	38
4.1.2 Laser Sheet Energy Distribution	39
4.2 Calibration Methodology.....	41
4.3 Calibration of LII Images	46
5 Conclusions.....	54
6 Future Work	57
7 References.....	58
8 Appendices	64
8.1 Pressure Vessel Window Assembly.....	64
8.2 Pressure Build-up Methodology.....	65
8.3 LII Measurements: Operating Procedure.....	66
8.4 LII Wiring Schematic	67
8.5 IPLab Settings	68
8.6 Average Extinction Data.....	69

List of Figures

Figure 1: Transmission electron micrograph of soot aggregates from ethylene counter-flow diffusion flame (Gaydon & Wolfhard, 1970).....	4
Figure 2: Co-flow burner	11
Figure 3: High pressure vessel.....	13
Figure 4: Ignition system electrode	14
Figure 5: Ignition system schematic.....	15
Figure 6: Unstable methane-air flame structure at (a) 4 atm, (b) 8 atm, (c) 16 atm, (d) 25 atm.....	18
Figure 7: Methane-air flame at 16 atm (frames from 12 second video clip).....	19
Figure 8: Methane-air flame structure at (a) 1 atm, (b) 2 atm, (c) 25 atm	22
Figure 9: Soot accumulated from high pressure ethylene-air flame.....	23
Figure 10: LII optical set-up	25
Figure 11: Optical schematic for extinction measurements.....	28
Figure 12: Path length of extinction measurement for methane-air and ethylene-air flames at 65% of 1 atm flame height on log-log scale.....	29
Figure 13: Transmission of laser extinction measurement at 65% of flame height at 1 atm	30
Figure 14: Path averaged soot volume fraction versus pressure at 65% and 85% of the flame height at 1 atm.....	32
Figure 15: Path averaged soot volume fraction versus pressure on log-log scale	33
Figure 16: Integrated $f_{sv,ave}$ versus pressure on a log-log scale for ethylene-air flames.....	34
Figure 17: Emissive power versus pressure on a log-log scale for a methane-air flame at pressures up to 50 atm (Miller & Maahs, 1977)	35
Figure 18: Methane-air flame at (a) 2 atm and (b) 4 atm; scaled to maximum signal of 962 (red)	36
Figure 19: Methane-air flame at (a) 8 atm, (b) 16 atm, (c) 25 atm; scaled to maximum signal of 6164 (red).....	37
Figure 20: Ethylene-air flame at (a) 1 atm and (b) 2 atm; scaled to maximum signal of 1489 (red)	37
Figure 21: Ethylene-air flame at (a) 4 atm, (b) 8 atm, and (c) 16 atm; scaled to maximum signal of 20703 (red).....	38
Figure 22: Knife-edge device	39
Figure 23: Energy distribution of laser sheet	40
Figure 24: Decomposition of flame into J concentric rings (Choi & Jensen, 1998).....	43
Figure 25: (a) Uncalibrated and uncorrected LII image and (b) calibrated and corrected LII image of ethylene-air flame at 16 atm.....	47
Figure 26: Soot volume fraction in methane-air flame at 2 atm.....	48
Figure 27: Soot volume fraction in methane-air flame at 4 atm.....	48
Figure 28: Soot volume fraction in methane-air flame at 8 atm.....	49
Figure 29: Soot volume fraction in methane-air flame at 16 atm.....	49

Figure 30: Soot volume fraction in methane-air flame at 25 atm.....	50
Figure 31: Soot volume fraction in ethylene-air flame at 1 atm.....	50
Figure 32: Soot volume fraction in ethylene-air flame at 2 atm.....	51
Figure 33: Soot volume fraction in ethylene-air flame at 4 atm.....	51
Figure 34: Soot volume fraction in ethylene-air flame at 16 atm.....	52
Figure 35: Calibrated and corrected LII images of methane-air flame normalized to maximum f_{sv} of 25 atm case.....	53
Figure 36: Calibrated and corrected LII images of ethylene-air flame normalized to maximum f_{sv} of 16 atm case.....	53

1 Introduction

Because the overall equivalence ratio of combustion in a diffusion flame can be much lower than the premixed flammability limit, the fuel economy of a diffusion-flame-dominated device, such as a Diesel engine, is improved over that of a premixed-flame-device such as a homogeneous charge internal combustion engine. However, with this improvement in fuel economy comes the disadvantage of dramatically more soot production, which in turn causes increased soot loadings within the flame that affect the heat transfer characteristics of the flame, lowering the combustion efficiency. As soot is a sensitive indicator of the interactions between combustion chemistry and fluid mechanics, an examination of soot formation, especially at the elevated pressures that most practical combustion devices operate at in order to gain thermodynamic efficiency, will contribute to fundamental combustion knowledge.

1.1 Soot Formation

The formation of soot is the result of an ordered, but not fully understood, process. Efforts have been devoted to studying reaction mechanisms and chemical reaction pathways leading to the formation of soot (Frenklach, 2002; Richter & Howard, 2000). Before significant reductions in the amount of soot emitted from diffusion controlled combustion processes can be realized, more information about the soot formation process, particularly at physically relevant conditions, such as at elevated pressures, is required.

Diffusion flames are more likely than premixed flames to yield soot due to the

fundamental differences in the controlling mechanisms influencing each flame. A premixed hydrocarbon flame will yield soot if the flame system is deficient in oxidizer that is responsible for converting the hydrocarbon into CO and H₂ (Wagner, 1981). It has been experimentally shown that soot will be produced if the ratio of carbon to oxygen atoms, C/O, for the flame system is approximately greater than 0.5. If a non-soot-yielding ratio of C/O is maintained throughout the mixture region, soot will not be produced. In a diffusion flame, the combustion process is diffusion controlled as the fuel and oxidizer originate from different sides of the reaction zone; furthermore, in contrast to a premixed flame in which the fuel is heated in the presence of an oxidizer, in a diffusion flame the fuel undergoes thermally-induced decomposition or pyrolysis in the absence of an oxidizing species. Consequently, maintaining a non-soot-yielding ratio of C/O throughout the mixing region is very unlikely for a diffusion flame and soot formation is more prevalent in this type of flame.

As the parent fuel molecules are transported via diffusion into the preheat zone, the elevated temperatures cause the large molecules to thermally decompose into smaller hydrocarbon fragments. After the pyrolysis of a non-aromatic fuel, precursor monoelements, namely acetylene (C₂H₂), are formed. The amount of soot produced by a given non-aromatic fuel is influenced by how easily the fuel can be converted to C₂H₂. For example, the pathway from a methane molecule to an acetylene molecule involves many more reactions than the pathway from ethylene to acetylene. As a result, ethylene produces more soot than methane. The pathway from precursor monoelements to soot continues

with three C_2H_2 molecules combining into a benzene ring, C_6H_6 . Several benzene rings then group together generating polycyclic aromatic hydrocarbons (PAHs). The PAHs are multi-benzene ring structures, initially saturated. As these rings lose hydrogen atoms, which are oxidized to OH and eventually H_2O , and become unsaturated, a process called polymerization occurs and the ring structures begin to condense together. As polymerization continues, the ratio of carbon to hydrogen atoms increases and enough rings will eventually group together to form a small soot particle or spherule. Surface reactions on the spherule cause it to grow. For reasons still not understood, the spherules no longer grow after reaching diameters between 30 and 50 nm. The spherules then begin adhering together to form agglomerates. These agglomerates then combine to form clusters.

The formation of soot is countered by soot removal through oxidation. The oxidation of soot is observable in a simple candle flame. The yellow color of a candle is caused by the incandescence of hot soot. If the quality of the candle wax is high, most of the soot formed will be oxidized before diffusing across the flame front and the flame will not smoke. Carbon that is liberated from the flame is referred to in the literature as smoke while carbon that is oxidized within the flame is deemed soot. One of the early methods of examining soot formation in diffusion flames at elevated pressures was to observe what combination of fuel flow rate and pressure caused the flame to smoke, i.e. record the smoke point (McArragher & Tan, 1972).

Soot is composed of approximately 1% by weight of hydrogen atoms, which results in soot having an empirical formula of approximately C_8H . Soot is observed to be

composed of spherical particles arranged in roughly chain-like structures as shown in Figure 1. In fact, these agglomerates are fractal-like with a fractal dimension of approximately 1.8. The diameter of a spherical particle ranges from 10 to 200 nm, but the diameter is most commonly between 10 and 50 nm. The individual spherical particle is composed of approximately 10^4 crystallites, each of which consists of 5 to 10 sheets of carbon atoms. These sheets of carbon atoms have length and width dimensions of 2 to 3 nm and are made of approximately 100 carbon atoms (Palmer & Cullis, 1965).

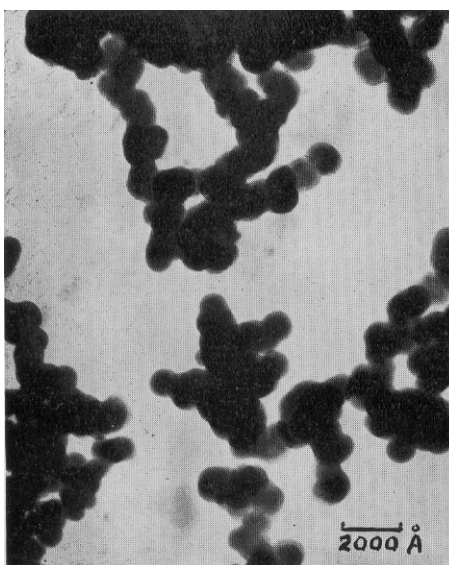


Figure 1: Transmission electron micrograph of soot aggregates from ethylene counter-flow diffusion flame (Gaydon & Wolfhard, 1970)

Due to the extremely small size of soot, it can be inhaled deeply into the lungs and its removal from the human air supply through filtering is difficult. Humans are regularly exposed to soot in transportation and industrial settings. Though the severity of these problems is debated frequently, it is widely acknowledged that soot causes health problems

in humans (Sydbom et al., 2001; Comstock et al., 1998; Morgan et al., 1997; Scheepers & Bos, 1992). Barfknecht (1983) details the historical progress of linking occupational soot exposure to its detrimental biological consequences. Additionally, Barfknecht examines the correlation between particulate air pollution levels and lung cancer mortality. This research indicates that polycyclic organic matter (POM), of which polycyclic aromatic hydrocarbons (PAHs) are a subset, is responsible for the mutagenic and carcinogenic properties of soot.

1.2 Effects of Elevated Pressure on Soot Formation

Most practical combustion devices operate at elevated pressures to increase thermodynamic efficiency, and consequently, it is important to examine the formation of soot under these conditions. It is well known that carbon formation increases while soot removal by oxidation declines with increasing pressure in diffusion-controlled devices (Flower & Bowman, 1986) and the rates of soot formation increase with increasing pressure (Flower, 1986). The mechanisms responsible for soot formation and oxidation at high pressures are significantly different than those active at low pressures. An exact, comprehensive explanation of these mechanisms and how they differ is still elusive, but it is generally agreed upon that elevating the pressure of a diffusion flame's ambient environment causes changes in the diffusion coefficient and reaction rate, which lead to more soot being produced.

The effect of elevated pressures on soot formation can be evaluated by measuring the soot mass yield as a function of pressure. One of the parameters that characterizes soot

mass yield is soot volume fraction (f_{sv}). Flower and Bowman (1986) made f_{sv} measurements in a laminar diffusion flame at elevated pressures up to 10 atmospheres using laser-scattering to examine the effects of pressure on soot formation and oxidation. The work of Flower and others indicates that increased pressure plays a significant role in increasing soot production in spray combustion, premixed flames, and diffusion flames (McArragher & Tan, 1972; Schalla & McDonald, 1955; Kadota et al., 1977; Miller & Maahs, 1977; Millberg, 1959; Fischer & Moss, 1998; Heidermann et al., 1999). Common diffusion-flame-devices operate at pressures between 25 and 30 atmospheres. The mechanisms responsible for soot formation at 1 or even 10 atmospheres may be drastically different than those prevailing at 30 atmospheres. Furthermore, Flower and Bowman collected line integrated f_{sv} values, which do not provide spatially or temporally resolved results. Tomography is one method that would provide spatially resolved f_{sv} , but this technique is limited in that it is time consuming and few high-pressure combustion devices provide the optical access required to employ tomography (Santoro & Shaddix, 2002).

Numerous models of soot formation in both premixed and diffusion flames at atmospheric and elevated pressures have been developed (Schittkowski et al., 2002; Zhang & Ezekoye, 1998; Kazakov et al., 1995; Hu et al., 2000). These models are typically empirical models requiring experimental data to determine appropriate fitting parameters. The development and refinement of experimental techniques aids in collecting quantitative, spatially and temporally resolved f_{sv} data that can be used to validate these models.

1.3 Laser Diagnostic Techniques

1.3.1 Laser Extinction

Energy is removed from a beam of light, such as a laser beam, when the beam passes through a molecule- or particle-filled medium. The molecules or particles scatter and absorb light from the beam, causing the beam to attenuate. Scattering and absorption in combination represent the phenomena of extinction (Van de Hulst, 1957). Extinction measurements have been used to determine path averaged soot volume fraction, $f_{sv,ave}$, and physical properties of soot, such as particle diameter and cluster size and structure.

If soot particles are assumed to be within the Rayleigh-scattering regime ($d \ll \lambda$), the following relation may be used to calculate a path averaged $f_{sv,ave}$ (D'Alessio et al., 1972)

$$f_{sv,ave} = \left(\frac{\lambda}{6\pi L} \right) \frac{\ln(I / I_o)}{\text{Im}\{(m^2 - 1)/(m^2 + 2)\}} \quad (1.1)$$

where I is the attenuated intensity, I_0 is the unattenuated intensity, m is the index of refraction of soot, and L is the path length. The attenuated intensity is the intensity measured in the presence of the flame while the unattenuated intensity is that without the flame. The index of refraction for soot was chosen to be $1.57-i0.56$ (Dalzell & Sarofim, 1969). The choice of index of refraction is a significant source of error and can affect

results by $\pm 40\%$. This particular index of refraction is generally accepted by the research community and was chosen so that comparisons could be drawn.

1.3.2 Laser Induced Incandescence

Laser Induced Incandescence (LII) capitalizes on soot primary spherules having diameters within the Rayleigh scattering regime and soot being an excellent absorber and, hence, emitter of radiation (Santoro & Shaddix, 2002). A brief, high energy laser pulse heats soot particles to near their vaporization temperature, ~ 4000 K, a temperature much greater than the temperature of the non-laser-heated soot within the flame, ~ 1800 K. Additionally, the wavelength of the thermal emission produced by the laser heated soot is blue-shifted in comparison to that of the non-laser-heated soot. The resulting incandescence can be collected by an intensified camera or other photodetecting device and used to determine qualitative and quantitative information about the soot field.

Over the last twenty years, the non-intrusive LII technique has proven itself to be a very versatile and important combustion diagnostic technique. Measurements of soot particle sizes (Bockhorn et al., 2002; Vander Wal et al., 1999; Starke & Roth, 2002; Will et al., 1995; Axelsson et al., 2000) and f_{sv} (Quay et al., 1994; Vander Wal & Weiland, 1994; Shaddix & Smyth, 1996; Bryce et al., 2000) can be made using LII in a wide range of experimental settings. The LII technique has not been utilized in diffusion flames at elevated pressures. LII is a timely and easily employed method that provides both spatially and temporally resolved f_{sv} .

Since Eckbreth (1977) and Melton (1984) first demonstrated the possibility of using laser heating to quantitatively measure soot particle characteristics, progress has not only been made in applying LII to new experimental conditions but also in finding the optimal LII operating conditions that provide the most reliable results. In pursuing this better understanding of LII, researchers have considered such issues as excitation intensity and wavelength (Vander Wal & Jensen, 1995), detection wavelength and integration time (Vander Wal, 1996), and the consequences of rapidly heating soot during LII (Vander Wal et al., 1995). In order to effectively utilize LII, much consideration must also be given to the calibration method. Several possible calibration methods have been demonstrated including light extinction (Choi & Jensen, 1998; DeCroix & Roberts, 2000; Axelsson et al., 2001; Bockborn et al., 2002; Vander Wal & Ticich, 1999) and gravimetric sampling (Vander Wal et al., 1996).

2 Experimental Apparatus and Conditions

2.1 Co-flow Diffusion Flame Burner

The burner used in this work produces the classic over-ventilated Burke-Schumman (1928) laminar diffusion flame. The burner geometry and flow rates were modified several times to achieve a stable laminar flame. Methane and ethylene were used in the experiments with air as an oxidizer. Methane was chosen because it is a simple hydrocarbon and represents natural gas, which is a very important commercial fuel. Ethylene was selected because it is a larger hydrocarbon with a much higher tendency to form soot. Ethylene was chosen as the representative larger hydrocarbon instead of the more commonly used propane because propane has a very low saturation pressure at room temperature and liquefies at pressures even moderately above atmospheric.

2.1.1 Burner Geometry

The co-flow diffusion flame burner had a height of 104 mm (Figure 2). Initially, the inner diameters of the burner's air co-flow and fuel tubes were 72.4 mm and 4.4 mm, respectively. To produce velocity-matched air and fuel flow rates with this geometry, the air flow rate required was greater than range of the air flow meters (0 to 50 SLPM) used in the experiment. Thus, a stainless steel insert was machined to reduce the diameter of the co-flow to 37.8 mm. The ratio of the diameters of the co-flow and fuel tubes was then approximately 8.5, which ensured that the mixing layer between the fuel and co-flowing air

was not influenced by the shear layer which forms between the co-flow and ambient air within the pressure vessel. Glass beads with a diameter of 4 mm filled the co-flow volume to aid in obtaining a uniform exit velocity profile. Steel wool was inserted in the fuel tube to create a pressure drop which made the fuel flow rate was less sensitive to pressure fluctuations upstream.

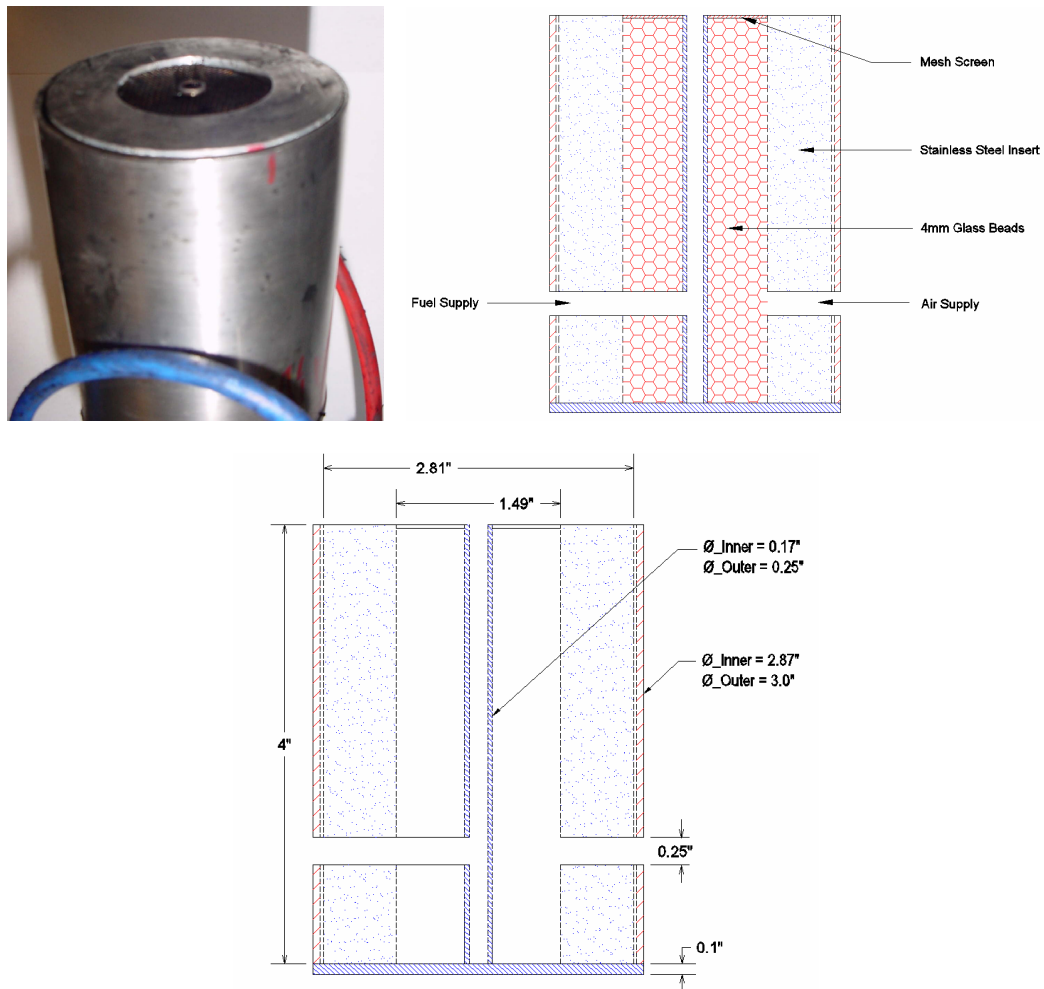


Figure 2: Co-flow burner

2.1.2 High Pressure Vessel

The burner was contained within a water-cooled pressure vessel (Figure 3), designed and originally built by Li (2001) and capable of continuous operation at pressures up to 30 atm (3.0 MPa). The vessel had a height of 1 m and four protruding flanges, three of which housed windows (7.6-cm diameter by 2.5-cm thick BK-7 glass) for observation and non-intrusive diagnostics. The burner had the ability to be translated vertically a distance of 7.5 cm within the pressure vessel so that different regions of the flame could be probed within the diameter of the window. The flame was relatively small compared to the volume of the chamber; therefore, air is used to purge the area surrounding the flame and the windows providing optical access. The collection of soot particles and water condensation in the interior volume of the pressure vessel and on the windows, which could have resulted in inaccurate data collection, was prevented by having additional air flow into the vessel as described in § 2.1.4. After burning fuels with a high propensity to soot, the windows were removed, cleaned, and reassembled as described in Appendix 8.1.

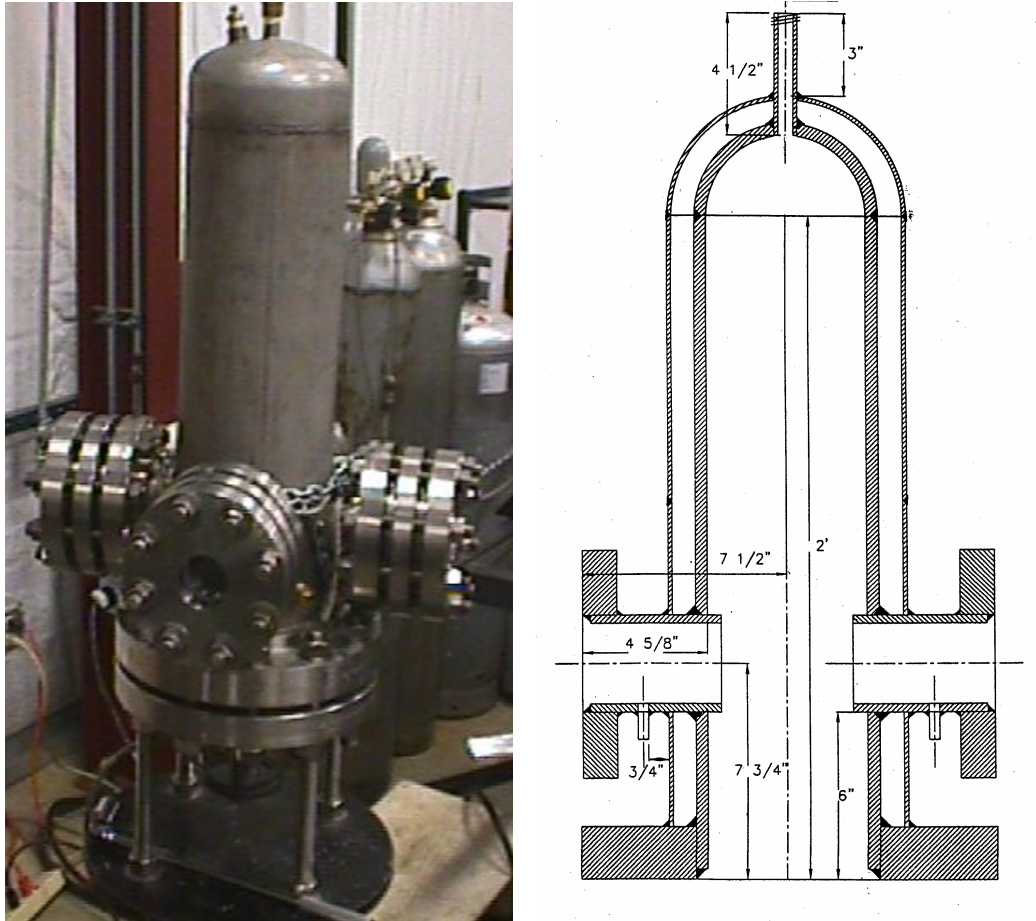


Figure 3: High pressure vessel

2.1.3 Ignition System

The fourth flange on the pressure vessel did not house a window for optical access. Instead a circular, stainless steel plate with several tapped holes seals the fourth flange. The ignition system's electrode was installed through one of these holes. The electrode consisted of a 63.5 mm diameter ceramic tube with a 16 mm inner diameter and a length of 32 cm (Figure 4). The ceramic tube passed through a screw that had been bored with a hole approximately 64 mm in diameter; the ceramic tube was fixed rigidly in place with a

high temperature, high pressure epoxy. A piece of stripped, twisted copper wire (approximately 5 strands) was threaded through the ceramic tube and extended about 3 cm and 0.5 cm from each end respectively. The wires protruding were then sealed to the ceramic tube with high pressure gasket maker.



Figure 4: Ignition system electrode

The electrode was screwed with Teflon tape surrounding the threads into the pressure vessel. The 3-cm long piece of wire inside the pressure vessel was positioned just millimeters from the fuel tube and was not allowed to have contact with any part of the burner or interior of the pressure vessel. The 0.5-cm long piece of wire extending from the outside of the pressure vessel was attached to a low-to-high voltage transformer via a high voltage BNC cable as shown in Figure 5. The low voltage supply to the transformer was a 12 V deep cycle marine battery. The positive terminal of the battery was connected to the transformer, and the negative terminal was grounded to the experiment. A contact switch between the battery and transformer allowed an arc of electricity to occur between the igniter wire inside the pressure vessel and the fuel tube. This spark was sufficient to ignite the burner reliably.

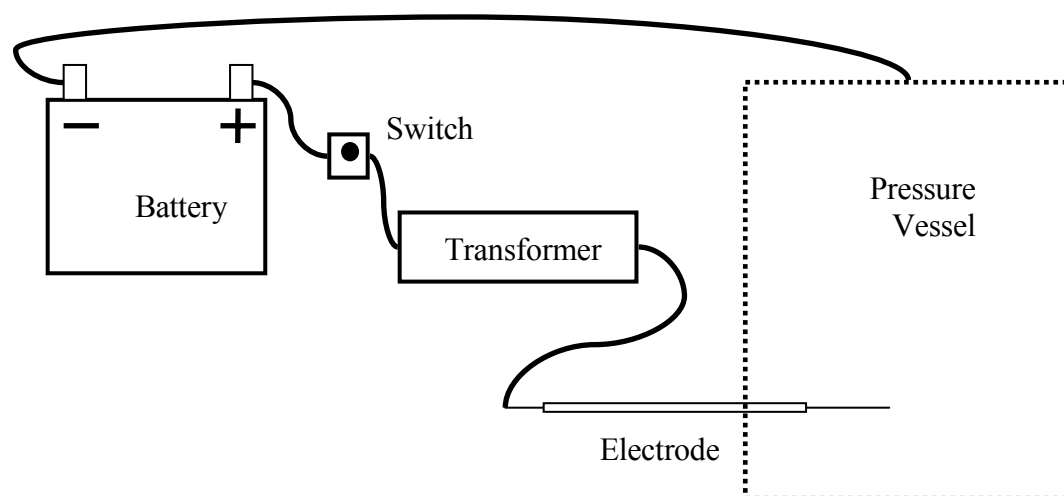


Figure 5: Ignition system schematic

2.1.4 Flow and Pressure Control System

Four entry ports for gases existed on the pressure vessel. Two were located on the bottom of the pressure vessel and supply the burner's fuel and air. The remaining two were located above two of the flanges housing windows and will hereafter be referred to as the "window ports." Air was supplied to the window ports for the dual purposes of preventing soot and water condensation from accumulating on the windows and aiding in increasing the pressure within the vessel.

The air for both the burner and the window ports was supplied from four tanks of dry, hydrocarbon-free bottled air with a purity of 99.9%. During operation of the burner at elevated pressures, the pressure differential on the regulator was adjusted so as to remain approximately 50 psi greater than the pressure within the vessel. The supply line from the two-stage regulator was bifurcated with each branch leading to a separate Hastings Model

201 flow meter with a 0-50 standard liter per minute (SLPM) range. The fuel flow rates required were much lower than those for the air supplies; thus the fuel flowed from the fuel bottle through a second two-stage regulator and a Hastings Model 200 flow meter with a 0-1000 standard cubic centimeter per minute (sccm) range. The purities of the methane and ethylene fuels were 99.0% and 99.5%, respectively. A Hastings Model 40 Power Supply provided both power to all three of the flow meters and a digital read-out of the flow rates for each meter. The flow meters were calibrated with nitrogen and thus a gas correction factor (GCF) was entered into the power supply for each gas. The GCFs provided by the manufacturer for air, methane, and ethylene were 0.9980, 0.7700, and 0.6040, respectively.

The fuel and air flow rates were kept constant as the pressure was increased within the vessel. For the methane-air flame at pressures ranging from 1 atm to 8 atm, the fuel flow rate was 0.100 SLPM, while the air flow rate was 20.0 SLPM. For the higher pressure flames, the fuel and air flow rates were increased to 0.150 SLPM and 30 SLPM in order to maintain an approximately constant flame height of 20 mm. The fuel and air flow rates for the ethylene-air flame were 0.060 SLPM and 20.5 SLPM, respectively. The value of the flow rates and the ratio of the fuel flow rate to the air flow rate greatly influenced the appearance and behavior of the flames, especially the stability as described in § 2.2.

Increasing the pressure within the vessel was achieved by increasing the flow rate of the window port and simultaneously decreasing the flow rate of the exhaust by adjusting the needle valve on the exhaust port. In order to consistently replicate flame characteristics at a given pressure, a very specific methodology was used to increase the pressure within

the vessel (Appendix 8.2). In general the flow rate to the window ports was increased first, followed by slowly decreasing the exhaust flow rate to achieve a given pressure. If changes in the pressure differentials on the regulators were required, the adjustment was made prior to increasing the window ports' flow rates. Great caution was exercised when making adjustments to any of the flow rates because operating under increased pressure made the flame more likely to suddenly extinguish. As the pressure was increased, reaction rates also increased while the diffusion rates remained relatively constant. The resulting flame had a thinner reaction zone and greater sensitivity to perturbations, i.e. if hydrodynamically disturbed, the flame was more likely to extinguish because diffusion of reactants cannot occur quickly enough to reestablish the flame (Miller & Maahs, 1977). The pressure within the vessel was displayed on an external gauge having a range of 0 to 1000 psig.

2.2 Physical Appearance of Flame

In the initial effort to maintain a flame at elevated pressures, the flow rates of the burner's fuel and air supplies were velocity-matched. If the flow rates were velocity-matched a mixing region existed without any shearing forces and all diffusion could be assumed to occur in the radial direction with no axial component. Additionally, during the initial efforts, the fuel and air flow rates used were much greater; at atmospheric pressure, the fuel flow rate was 0.5 SLPM while the air flow rate was 35.7 SLPM. At these higher, velocity-matched flow rates, the height of the flame was much more sensitive to pressure increases. It was desired to maintain a constant flame height of about 6 cm as this height is

typical of laboratory flames that have been studied by others and offers better spatial resolution of the soot field. As the pressure was increased, the flow rates of the fuel and air were raised as well to maintain the constant flame height. At pressures nearing 25 atm, the velocity matched fuel and air flow rates were 1.0 SLPM and 71.43 SLPM. Under these conditions, the flame maintained a constant height and had velocity matched flow rates, but it was very unstable at pressures greater than 4 atm as depicted in Figure 6.

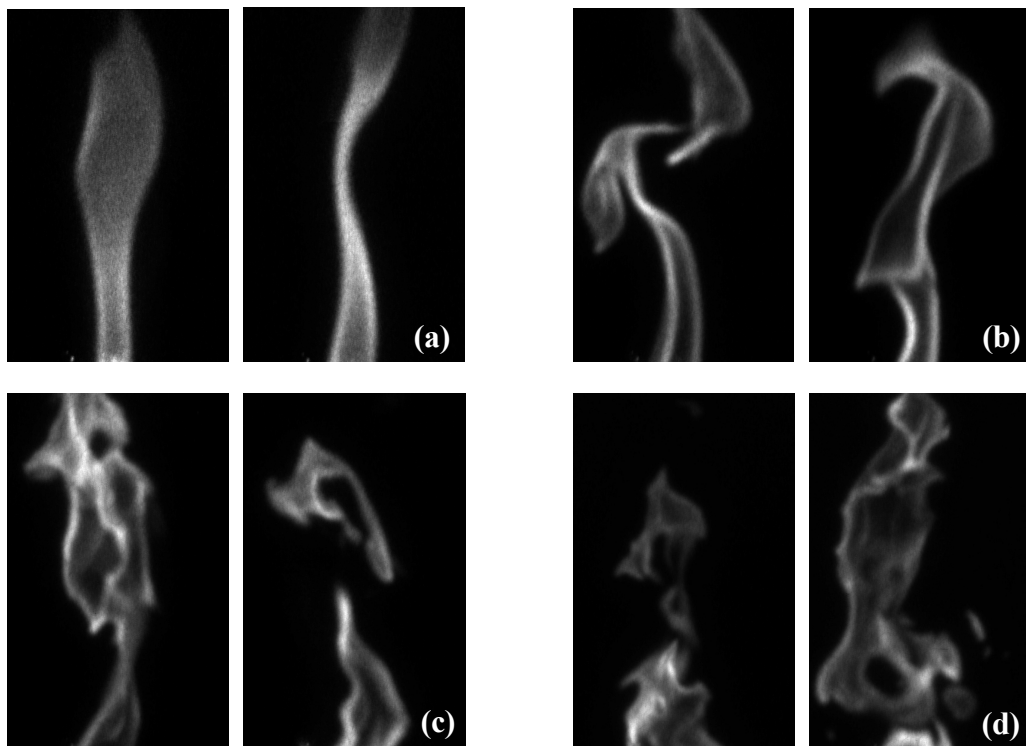


Figure 6: Unstable methane-air flame structure at (a) 4 atm, (b) 8 atm, (c) 16 atm, (d) 25 atm

At pressures of 1 atm and 2 atm, the flame maintained the conventional over-ventilated, candle flame-like shape. Above 2 atm, the flame began to wrinkle and the

flame front was significantly contorted. Flame pockets began to break from the primary flame as shown in Figure 7. This figure shows six frames from a video of a methane-air flame operating at 16 atm. The vortical shapes and pocket formations are very prominent.

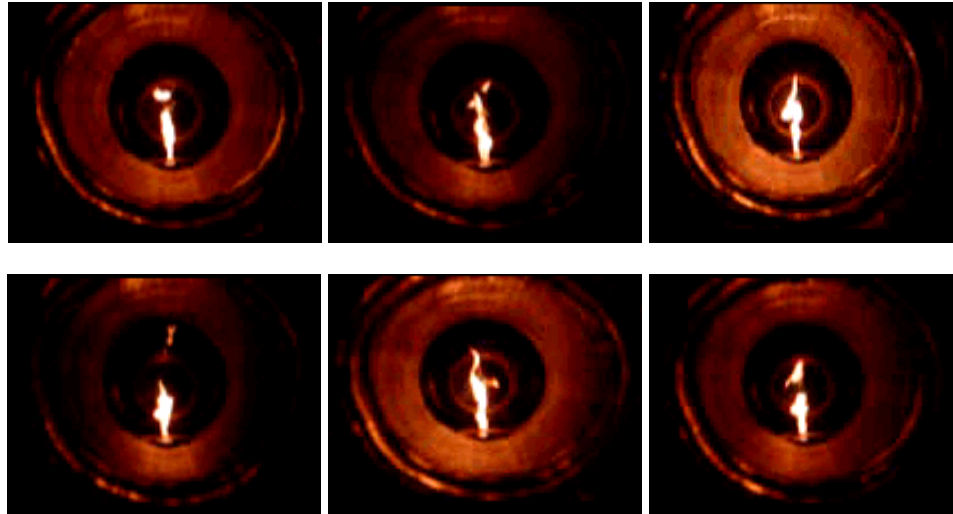


Figure 7: Methane-air flame at 16 atm (frames from 12 second video clip)

This highly unstable and distorted flame was not desirable as one of the assumptions of the calibration and correction methodology (described in § 4.2) is an axisymmetric flame shape. This instability can be attributed to the increased effects of buoyancy associated with elevated pressures. In addition to becoming more contorted with increasing pressure, the flame was also observed to be producing more soot as expected and as evidenced by an increase in flame luminosity due to the naturally occurring incandescence of soot particles.

Flower & Bowman (1986) and Miller & Maahs (1977) have done the majority of research on soot production in laminar diffusion flames at elevated pressures. As stated in § 1.2, the work of Flower & Bowman was performed up to a maximum pressure of 10 atm and evaluated an ethylene-air flame. To achieve a stable, axisymmetric flame at pressures greater than 2 atm, Flower and Bowman used fuel flow rates ranging from 0.102 to 0.294 SLPM, with an air flow rate of 252 SLPM at 1 atm (Flower & Bowman, 1986). The fuel flow rates used by Flower and Bowman were much lower than those used to generate the previously discussed unstable flame in the present work, and the air flow rate was significantly greater. Flower & Bowman described their flame as being “greatly overventilated” and stated that “this air flow is 60 times the stoichiometric requirement for the highest fuel flows studied.” It was theorized that this overventilation helped to maintain a stable flame structure, but unfortunately, with the air flow meters and air supply system used in this work such high air flow rates could not be achieved, particularly at higher pressures. This proposed connection between extreme overventilation and flame stability was further supported by the work of Miller and Maahs (1997), who studied nitrogen oxide (NO_x) formation in a laminar methane-air diffusion flame at pressures up to 50 atm. The burner used by Miller and Maahs (1997) had a fuel tube diameter of 3 mm and an air co-flow diameter of 20.5 mm. The fuel and air flow rates were 0.0418 SLPM and 2.45 SLPM. These flow rates were not velocity matched for the given burner geometry; the air flow rate was 1.4 times greater than the air flow rate required to match the velocity of a 0.0418 SLPM fuel flow rate.

Beginning with the relationship between the fuel and air flow rates used by Miller and Maahs and experimenting with the burner of the present work, it was determined that for the methane-air flame to remain stable at pressures approaching 25 atm, the air flow rate needed to be 20 SLPM, or 2.8 times the air flow rate required to match the velocity of a 0.1 SLPM methane flow rate. Similarly for the ethylene-air flame, it was determined that an air flow rate of 20.5 SLPM, 4.7 times the air flow rate required to match the velocity of a 0.06 SLPM ethylene flow rate, would produce a stable flame.

Observations on the effects of pressure on the physical characteristics of the flame were similar to those made by Miller and Maahs (1977). In their work, they also noted that the flame was wide and convex at 1 atm, and as the pressure increased, the flame became thinner and more concave. It was also observed that the naturally occurring soot incandescence increased with pressure. Figure 8 shows the flame at 1, 4 and 25 atm. The blue zone is indicative of O₂ Schumann-Runge radiation and CO + O continuum radiation while the brighter blue zones on the sides and near the fuel tube is evidence of C₂ and CH radiation (Gaydon & Wolfhard, 1970). The yellowish-white region is a result of soot luminosity; as the pressure was raised, this region became more orange and spread downward towards the base of the flame. The orange color of the flame indicates that its temperature was between 1200 and 1500 K. As the pressure was increased to 25 atm, the trend of decreasing flame diameter and increased soot luminosity was consistent. Due to the increased presence of soot acting as a reaction intermediary within the flame at elevated pressures, the reaction mechanisms at the higher pressures are different than those at

atmospheric pressure, which may explain the significant change in flame shape with increasing pressure; comparatively, soot particles are higher in mass than other combustion products and cannot diffuse away from the primary flame region as a gaseous product might. Combustion must then be maintained by oxygen diffusing inward to the primary flame region, resulting in a narrowing flame structure (Miller & Maahs, 1977).



Figure 8: Methane-air flame structure at (a) 1 atm, (b) 2 atm, (c) 25 atm

The fuel and air flow rates also influenced the height of the flame. The flow rates chosen to ensure flame stability resulted in a flame height of approximately 20 mm or 5 times the inside diameter of the fuel tube.

As expected, the ethylene-air flame produced much more soot than the methane-air flame. This was evident in the flame appearance, as the orange color associated with soot incandescence appeared in a greater portion of the ethylene-air flame than in the methane-air flame at a given pressure. As discussed in § 2.4, the transmission of the extinction laser beam decreased more dramatically with increasing pressure for the ethylene-air flame. In

the ethylene-air flame at pressures of 16 atm and above, soot accumulated around the fuel tube exit (Figure 9). As a consequence, no LII data was taken for the ethylene-air flame above 16 atm.

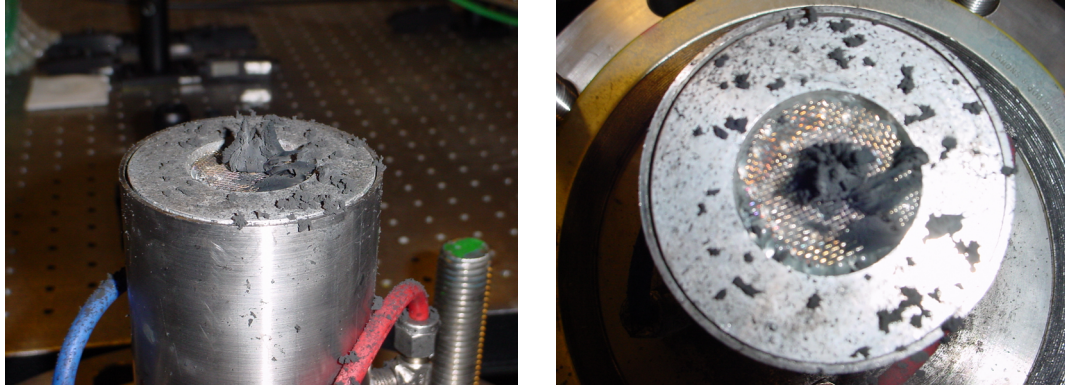


Figure 9: Soot accumulated from high pressure ethylene-air flame

2.3 Laser Induced Incandescence

Spatially and temporally resolved measurements of f_{sv} are desired in order to determine such physical processes as the rates of primary particle formation, clustering, cluster-cluster agglomeration, and oxidation in diffusion flames. To obtain spatially resolved, instantaneous f_{sv} measurements, Laser Induced Incandescence (LII) is employed. Briefly, the LII technique utilizes a very short duration output from an Nd:YAG laser to heat soot particles to near their vaporization temperatures. The thermal radiation emitted from these heated particles can then be related quantitatively to their volume fraction with appropriate calibration. This technique provides spatially resolved and instantaneous f_{sv}

measurements. An operating procedure for the combined use of the burner and LII technique is given in Appendix 8.3.

2.3.1 Optical Set-up

The 1064 nm output from a Continuum Minilite PIV laser was used to heat the soot particles (the doubling crystal from the laser was removed such that the first harmonic of the laser output was used); this particular wavelength was used to eliminate possible photochemical interferences (Vander Wal, 1996) since the 1064 nm photon is not so energetic as to cause fluorescence of intermediate species, such as PAHs. The output from the laser was formed into a sheet prior to entering the region of interrogation (Figure 10). The sheeting forming optics had an anti-reflective coating for the infrared region. The beam was first collimated with a plano-concave lens ($f = -50$ mm, $\phi = 12.7$ mm) and plano-convex lens ($f = 300$ mm, $\phi = 50.8$ mm) and then collapsed into a laser sheet with a cylindrical convex lens ($f = 400$ mm, 30 mm x 60 mm). This combination of optics produced a laser sheet with a height of 37 mm and a thickness of 300 μm . The laser's power was measured, and with the laser sheet dimensions, the laser fluence was found to be 0.30 J/cm^2 . A laser fluence of 0.30 J/cm^2 is within the "plateau region" of LII excitation, i.e. above a certain energy threshold, the LII signal emitted from heated soot particles becomes insensitive to the laser fluence. The plateau region has an upper bound; Vander Wal and Jensen (1998) found that a laser fluence greater than 0.50 J/cm^2 causes changes to the soot morphology and possibly vaporization of the soot particles.

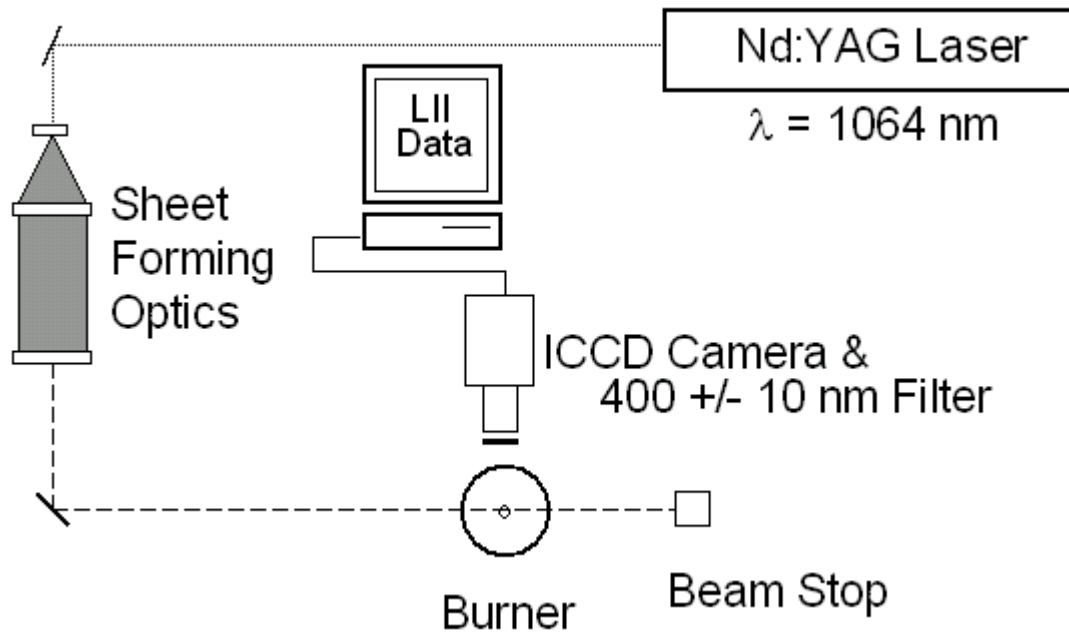


Figure 10: LII optical set-up

The LII signal was collected with a Princeton Instruments ICCD camera. Careful consideration was given to the filter used with the intensified camera as collection of flame luminosity signal was to be minimized. It was determined that a 400 nm +/- 10 nm filter eliminated the majority of signal due to flame luminosity even with the burner operating at elevated pressures. The maximum gain of the camera is 10.0 and for LII image acquisitions in this work, the gain was set to 9.0. The image collection software used was IPLab (see Appendix 8.5 for settings). Ten LII images were acquired at each pressure. Each image had a size of 265 pixels by 426 pixels; each pixel was equal to 63 μm (~16 px/mm).

2.3.2 *Timing and Wiring*

A SRS DG-535 digital delay generator served as the master clock for the LII measurements and provided TTL signals to the laser that commanded a given laser event, such as flash lamp or Q-switch activation (Appendix 8.4). The internal trigger of the DG-535 was set at 10 Hz. This repetition rate was chosen because the Nd:YAG laser operates between 8 and 15 Hz. Thus a command, T_0 , was sent to the laser flash lamps at an approximate rate of 10 Hz. The laser Q-switch was activated 160 μ sec after the flash lamps (positive going AB TTL = $T_0 + 160 \mu$ sec). The DG-535 also triggered the Princeton Instruments PG-200, the camera gate controller, at 150 μ sec after a flash lamp signal (positive going CD TTL = $T_0 + 150 \mu$ sec); the PG-200 then activated the Princeton Instruments ST-130 camera controller that coordinated image acquisition between the camera and the Macintosh computer used to store data. The PG-200 provided an interface to set the camera gate width and delay relative to the laser pulse. It was desired that the acquisition event, i.e., the camera gate opening, occur simultaneously with the laser pulse passing through the region of integration. This operating condition is known as prompt detection and is generally favored as it prevents biasing of the LII signal that can occur due to varying primary particle sizes and temperature gradients within the flame region (Bryce et al., 2000; Vander Wal, 1996). To monitor the laser firing event, scattering from a turning mirror was collected by a photodiode. This signal and the pulse monitor signal from the PG-200 were displayed on an oscilloscope to ensure the two events were temporally coincident. The delay on the PG-200 was adjusted to 9985 ns to give the best

overlap of laser and acquisition events. A gate width of 30 ns was used in the present work. DeCroix and Roberts (2000) found that a gate width of 30 ns provided acceptable signal-to-noise ratios for even the low soot yielding methane-air flames without biasing the data towards larger particles; the larger particles cool more slowly than smaller particles that have a larger surface area to volume ratio. The LII signal of smaller particles decays more quickly.

2.4 Extinction Measurements

Calibration of the LII signal required measuring the extinction ratio of a second lower-powered laser. A Helium-Neon (HeNe) laser and photodiode were used to provide this extinction measurement. The HeNe laser was chosen for extinction measurements because DeCroix and Roberts (2000) expressed concern about using the 488 nm wavelength light from an Argon ion laser since the large scattering component associated with that wavelength causes an over prediction of calibration factors. The beam passed through a chopper set at 300 Hz and a plano-convex focusing lens before reaching two turning mirrors (Figure 11). The first mirror reflected approximately 25% of the beam's intensity through the pressure vessel windows without encountering the flame. The signal from this beam is collected by a photodiode and accounted for any soot build up within the pressure vessel and/or on the windows and any energy fluctuations in the laser beam. The second mirror reflected the remaining beam through the pressure vessel and directly over the center of the fuel tube at a known height above the fuel tube. Before reaching their respective photodiodes, each beam passed through a 632.8 nm laser line filter to eliminate

the considerable influence of flame luminosity on the collected signal. An oscilloscope then digitized and temporally averaged the signal collected by the photodiodes.

Extinction measurements were taken for both methane-air and ethylene-air flames at approximately 65% of the 1 atm flame height or 10 mm above the burner for the second set of experiments when the flame was stable and shortened in height. Additional extinction measurements were taken with the methane-air flame at 85% of the flame height.

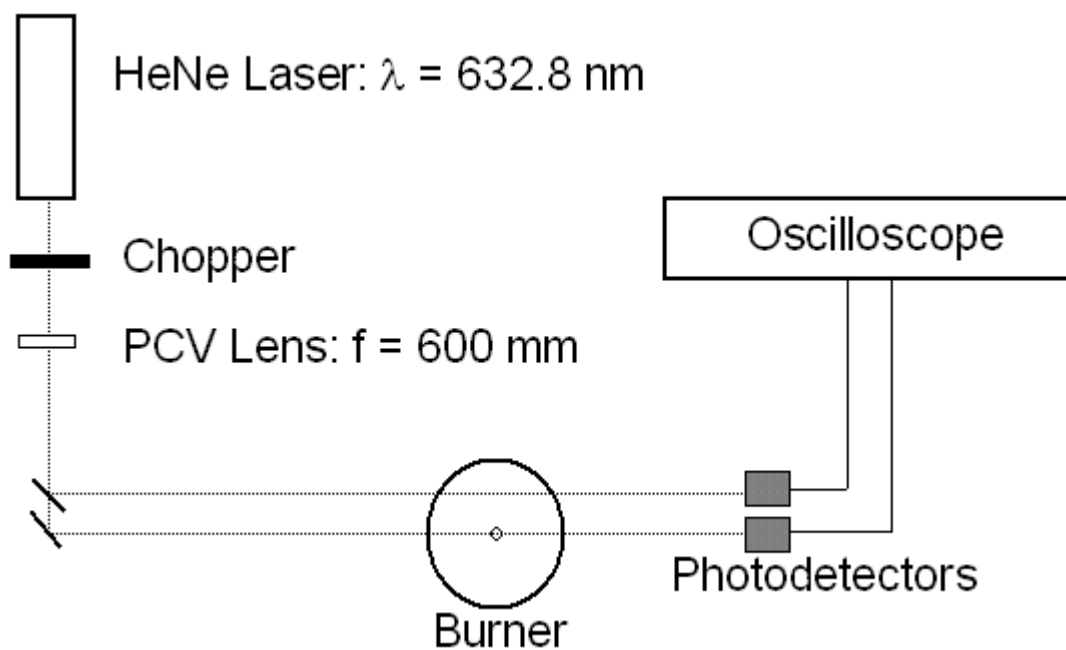


Figure 11: Optical schematic for extinction measurements

Since this extinction measurement is an integrated value, the path length must be known accurately. Concurrently with the extinction measurements, images of the flame

were taken with the intensified camera. The exact pixel location of the laser beam's passing was known and the path length was measured at that height. As Figure 12 shows, the path length decreased with increasing pressure, indicative of the narrowing effects pressure has on flame shape. The path length of the methane-air flame scaled with pressure as $p^{-0.46}$ and the path length of the ethylene-air flame as $p^{-0.57}$.

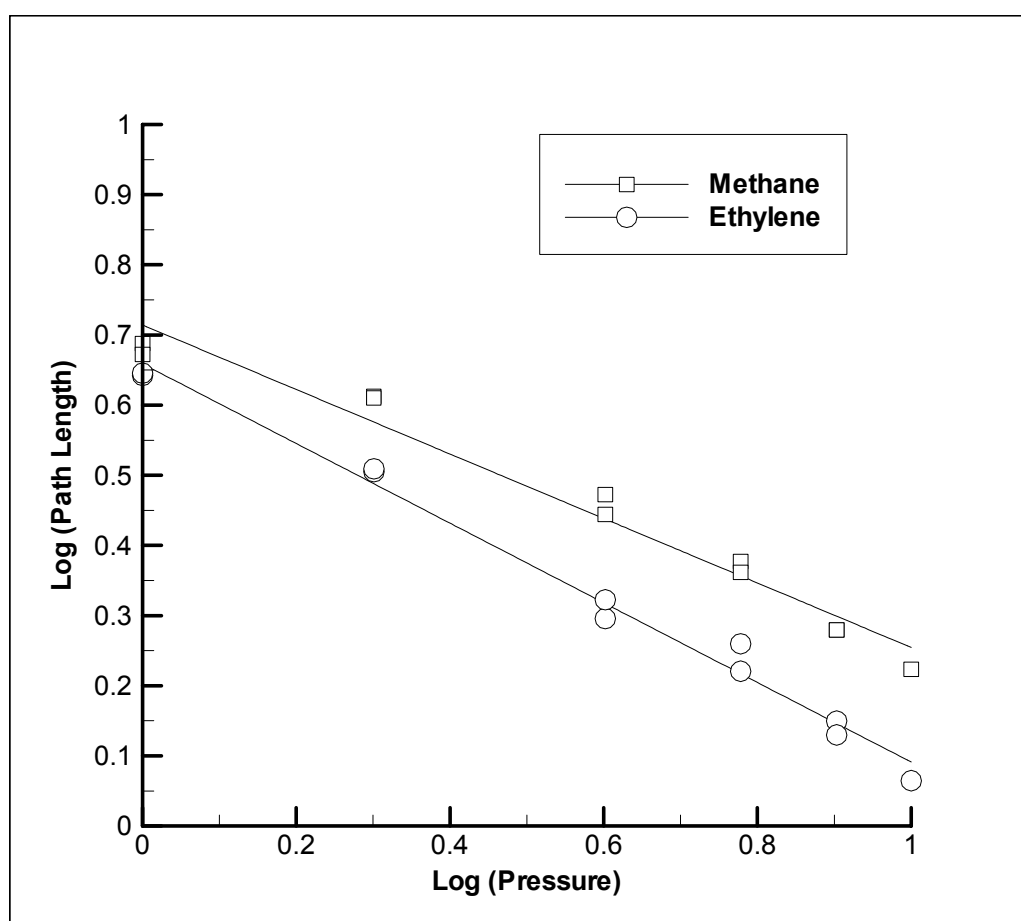


Figure 12: Path length of extinction measurement for methane-air and ethylene-air flames at 65% of 1 atm flame height on log-log scale

The extinction measurements were taken at pressures of 1, 2, 4, 6, 8 and 10 atm. Above this pressure, both the methane-air and the ethylene-air flames are no longer considered “optically thin,” i.e., the transmission of the laser beam approaches or drops below 80%. As Figure 13 shows, the ethylene-air flame rapidly deviates from the condition of being optically thin above pressures of 2 atm.

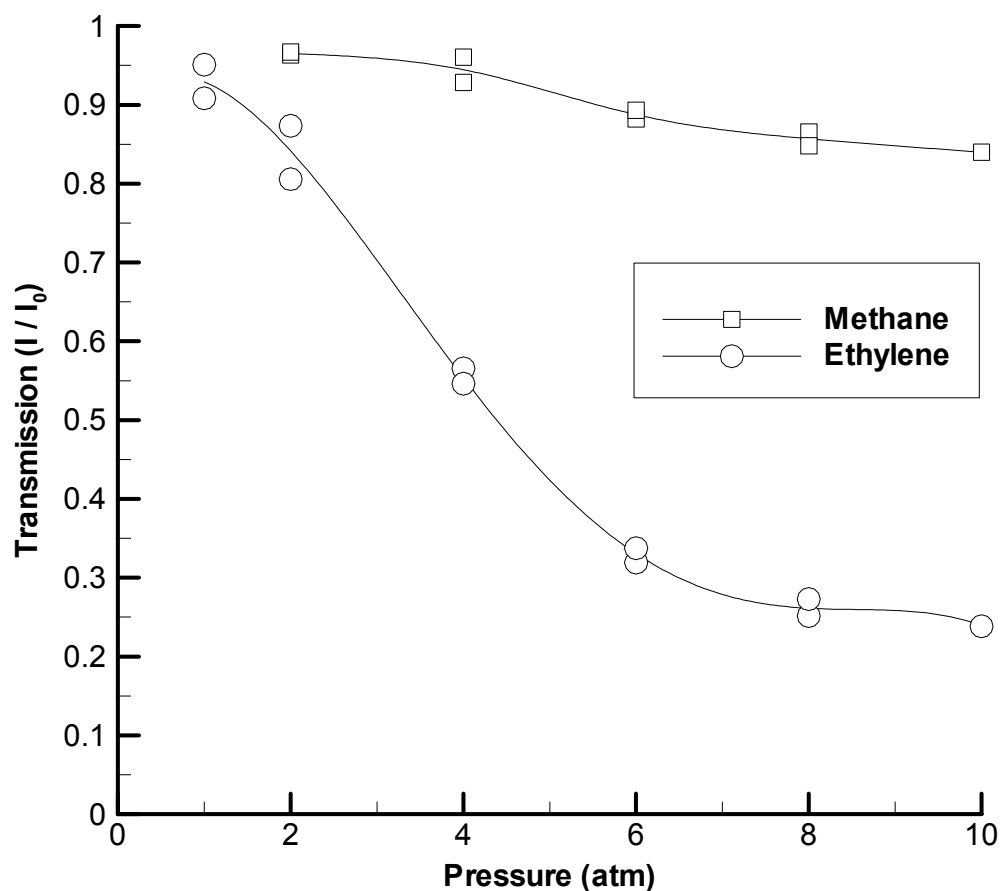


Figure 13: Transmission of laser extinction measurement at 65% of 1 atm flame height

3 Extinction Measurements and Soot Volume Fraction

3.1 Extinction Measurements as Calibration

The calibration procedure requires measuring the extinction ratio of a second lower-powered laser, knowing an accurate path length, and assuming an axisymmetric flame. The extinction ratio is the ratio of the signal of the attenuated beam to the signal of the unattenuated beam. The attenuated beam passes through the flame while the unattenuated beam does not. It is desired to use an extinction ratio that corresponds to an optically thin flame as described in § 2.4. The outcome of the calibration procedure is a calibration factor that relates LII signal intensity to soot volume fraction and ultimately leads to a quantitative image of f_{sv} throughout the flame (Choi & Jensen, 1998; DeCroix & Roberts, 2000). This correction factor found at a pressure yielding an optically thin flame can then be applied to the LII images taken at other pressure cases up to 25 atm.

3.2 Soot Volume Fraction

The extinction measurements collected for the calibration procedure were also used to calculate path averaged $f_{sv,ave}$ values at the height above the burner where the extinction measurement was taken as described in § 1.3.1. The majority of previous $f_{sv,ave}$ data taken at elevated pressures has been data of this nature. For comparison, these path averaged $f_{sv,ave}$ values were calculated for the methane-air flame at 65% and 85% of the flame height and for the ethylene-air flame at 65% of the flame height (Figure 14). As discussed in § 2.4, the extinction measurements were taken at pressures of 1, 2, 4, 6, 8, and 10 atm. The

path length was measured from images of the flame taken simultaneously with the extinction measurements.

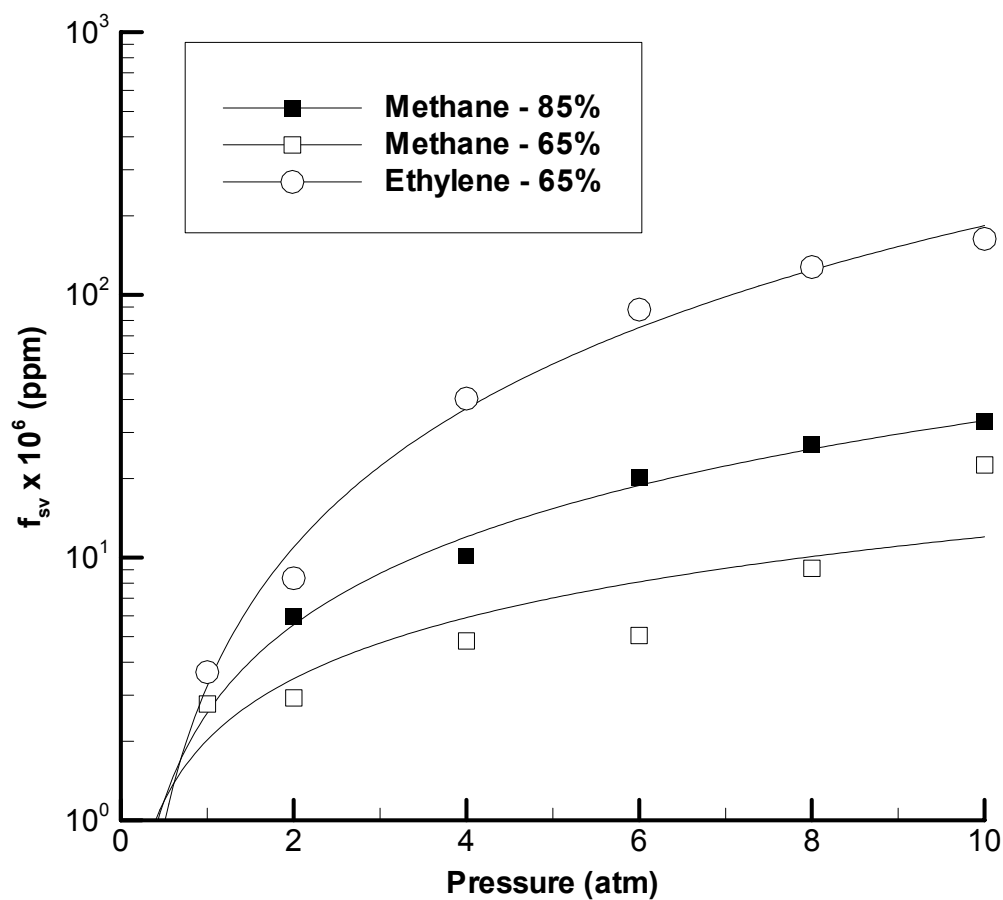


Figure 14: Path averaged soot volume fraction versus pressure at 65% and 85% of the 1 atm flame height

When $f_{sv,ave}$ is plotted versus pressure on a log-log scale (Figure 15), the slope of the linear fit line indicates a relationship between soot yield and pressure. It was found that

$f_{sv,ave} \propto p^m$, where m is the slope of the linear fit. For the methane-air flame at 85% of the flame height, $m = 1.1$; the methane-air flame at 65% of the flame height, $m = 0.77$; and the ethylene-air flame at 65% of the flame height, $m = 1.75$.

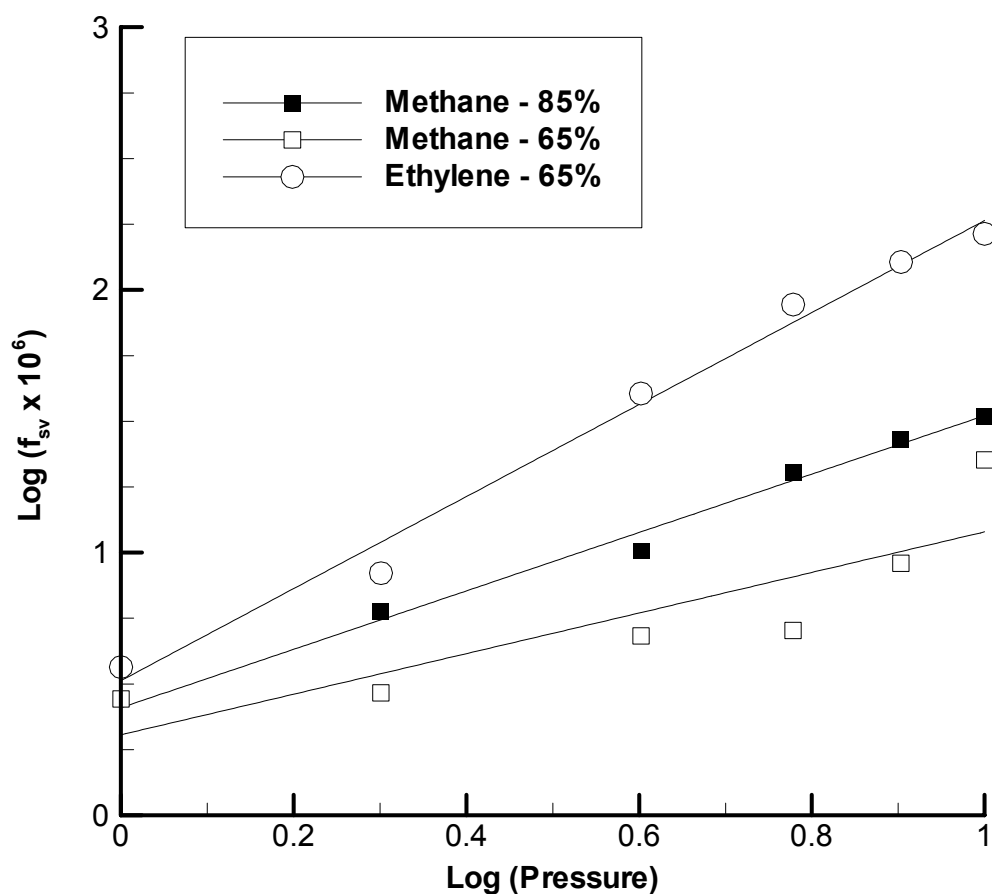


Figure 15: Path averaged soot volume fraction versus pressure on log-log scale

Flower and Bowman (1986) found a pressure dependence $m = 1.2 \pm 0.1$ for their ethylene-air flame at pressures up to 10 atm. They determined an integrated $f_{sv,ave}$ for

ethylene-air flames with a fuel flow rates of 1.7 scc/s, 2.4 scc/s and 3.9 scc/s. The $f_{sv,ave}$ values measured in the present work's ethylene-air flame, which has a fuel flow rate of 1.0 scc/s, were integrated and plotted along with the results of Flower and Bowman (1986) in Figure 16. The integrated $f_{sv,ave}$ values shown in Figure 16 were found at the same non-dimensional axial location. The integrated $f_{sv,ave}$ for the ethylene-air flame of the present work scaled with pressure as $p^{1.2}$. The integrated $f_{sv,ave}$ values of Flower and Bowman at 1.7 scc/s, 2.4 scc/s and 3.9 scc/s scaled as $p^{1.2}$, $p^{1.1}$ and $p^{1.0}$, respectively.

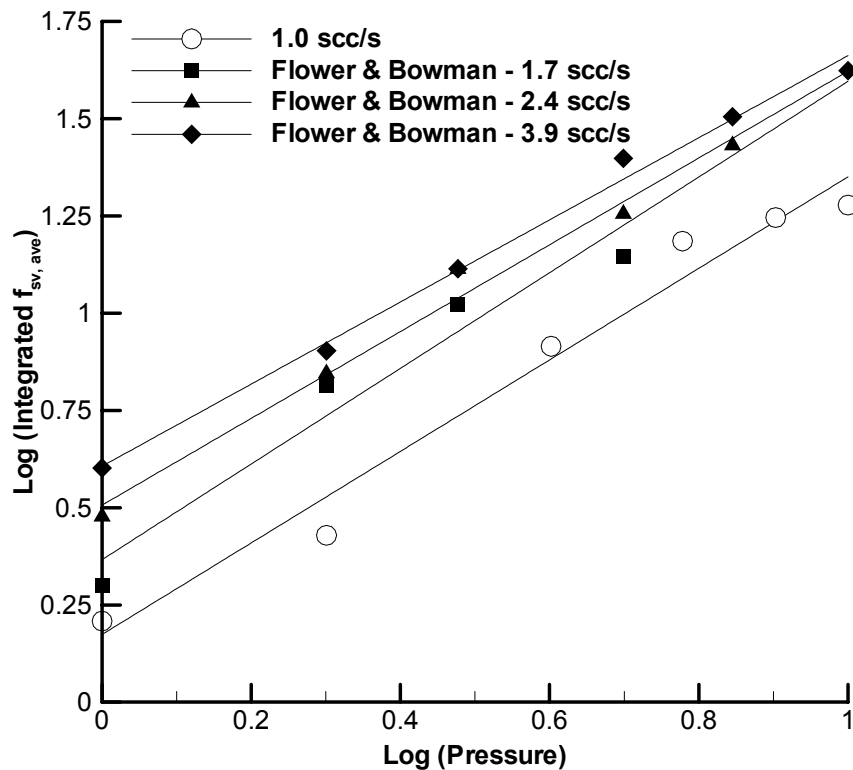


Figure 16: Integrated $f_{sv,ave}$ versus pressure on a log-log scale for ethylene-air flames

Some similar comparisons can be made with the work of Miller and Maahs (1977). While they did not explicitly measure $f_{sv,ave}$, they did measure the emissive power from the flame at pressures up to 50 atm. As shown in § 2.2, increasing luminosity is indicative of increasing soot presence within a flame. In examining Figure 17, it becomes evident that two pressure trends are present. The emissive power of the methane-air flame scaled as $p^{1.4}$ for pressures between 0 and 25 atm. As the pressure was increased above pressures of 25 atm, the emissive power and consequently $f_{sv,ave}$ have a decreased dependence on pressure, $p^{0.2}$.

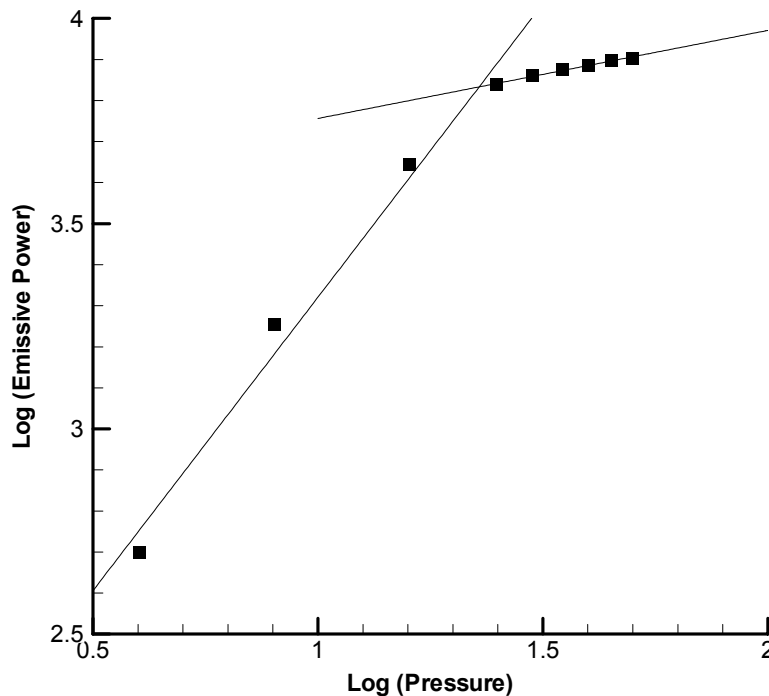


Figure 17: Emissive power versus pressure on a log-log scale for a methane-air flame at pressures up to 50 atm (Miller & Maahs, 1977)

4 Calibration of LII Measurements

4.1 Correction of Raw LII Signal

Before the calibration procedure began, the raw LII signals were corrected for both background noise and variations in the energy distribution of the laser sheet. Figures 18 through 21 show the uncorrected LII signals for the methane-air and ethylene-air flames at various pressures with the laser sheet moving from left to right. The effect of pressure on soot production is even evident in these uncorrected and uncalibrated images. The images are colored according to the signal value of each pixel. Note that the lower pressure cases are colored according to different scales as the change in signal values is so dramatic with increasing pressure – one order of magnitude for the methane-air flame and two orders of magnitude for the ethylene-air flame.

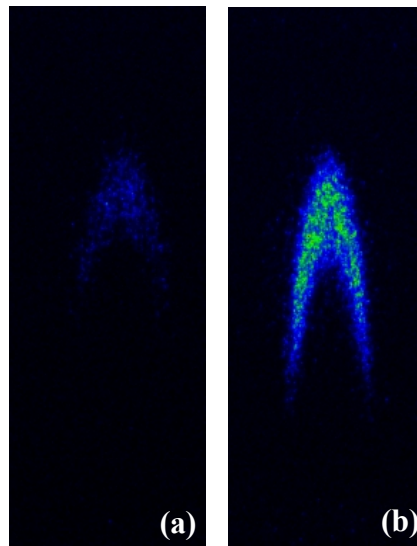


Figure 18: Methane-air flame at (a) 2 atm and (b) 4 atm; scaled to maximum signal of 962 (red)

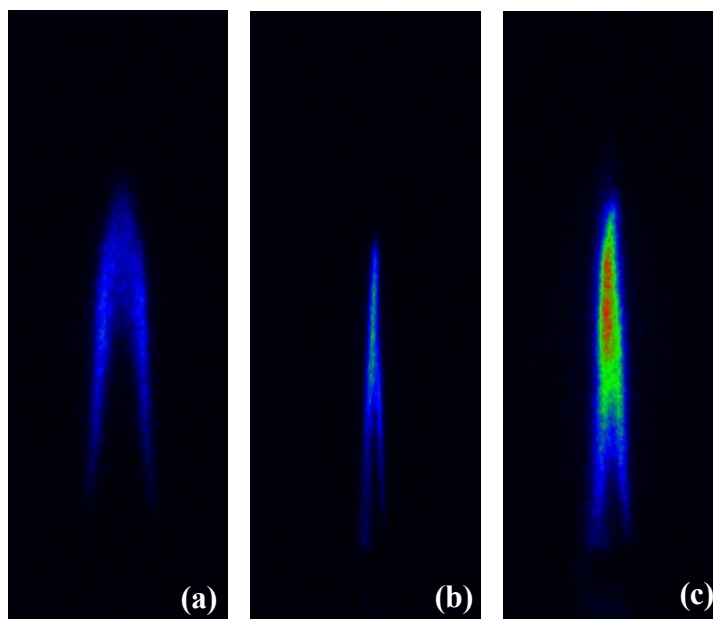


Figure 19: Methane-air flame at (a) 8 atm, (b) 16 atm, (c) 25 atm; scaled to maximum signal of 6164 (red)

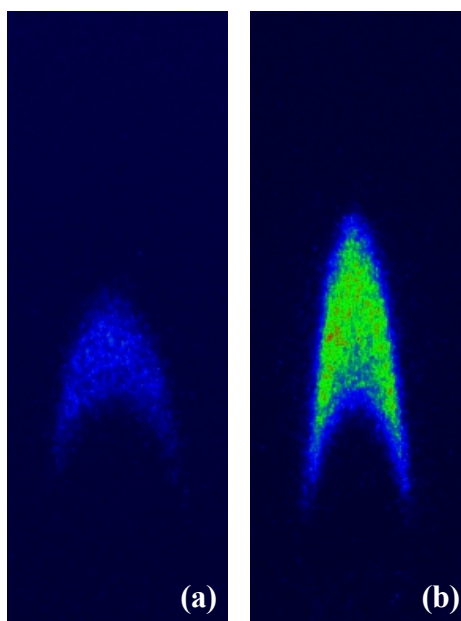


Figure 20: Ethylene-air flame at (a) 1 atm and (b) 2 atm; scaled to maximum signal of 1489 (red)

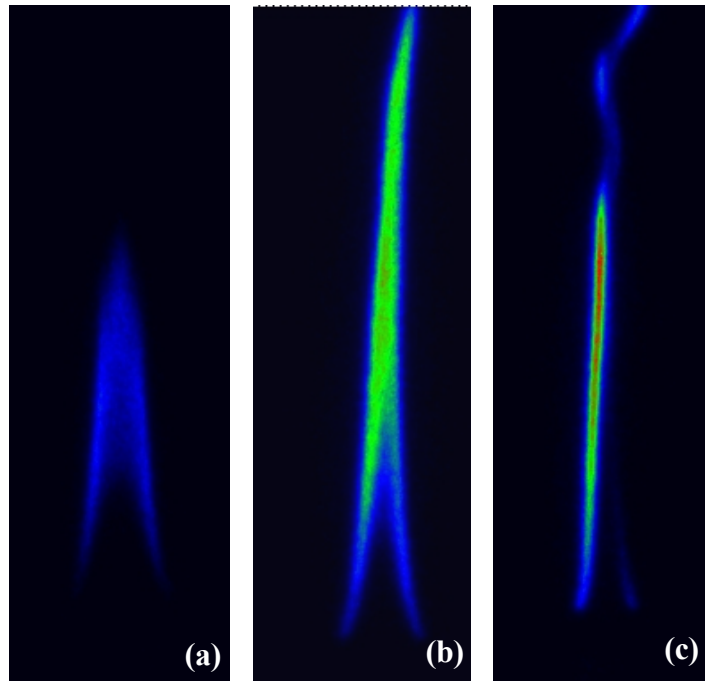


Figure 21: Ethylene-air flame at (a) 4 atm, (b) 8 atm, and (c) 16 atm; scaled to maximum signal of 20703 (red)

4.1.1 Background Noise

Variation in the camera dark current intensity was the only major source of background noise, as flame luminosity as a source of background noise was largely removed by using a narrow bandpass filter. The camera dark current intensity was a function of CCD temperature, which varies somewhat because the temperature of the ground water used for cooling is not constant. To account for the variations in dark current intensity, a set of 10 images were taken with the camera lens capped prior to any collection of LII data. These 10 images were then averaged and subtracted from the LII images.

4.1.2 Laser Sheet Energy Distribution

The distribution of energy through the laser beam is non-uniform and usually follows a Gaussian profile. When this nominally round beam is collapsed in one direction to form a sheet, the Gaussian profile becomes even steeper. To correct for this variation in energy distribution, a knife-edge with a precise translation device was fixed above the center of the fuel tube (Figure 22).

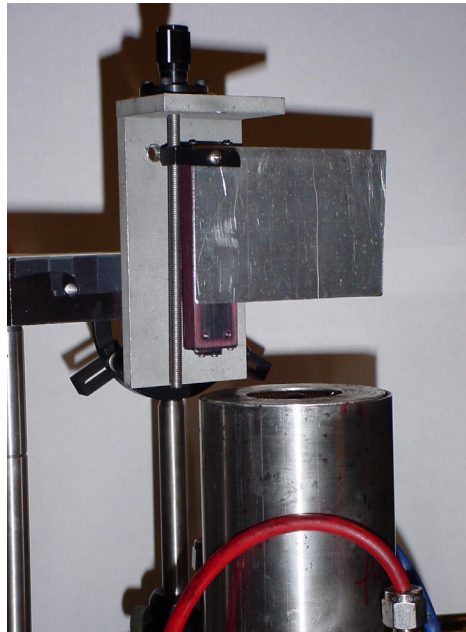


Figure 22: Knife-edge device

Initially, the knife-edge allowed the entire laser sheet to pass over the burner tube and through a convex lens that partially refocused the laser sheet to a size that would fit on the collection surface of an energy meter. The energy was recorded and the knife-edge was lowered a known distance. Another energy reading was then recorded and so on until the

beam was fully blocked. From the energy meter readings, a profile of the energy distribution of the laser sheet was determined. Several series of readings were taken and averaged to give the profile shown in Figure 23. Since the laser energy was not uniform across the sheet, different areas of the flame experienced variations in heating due to the laser. To correct the LII images for this discrepancy, each column of the LII image was divided by the profile shown in Figure 23.

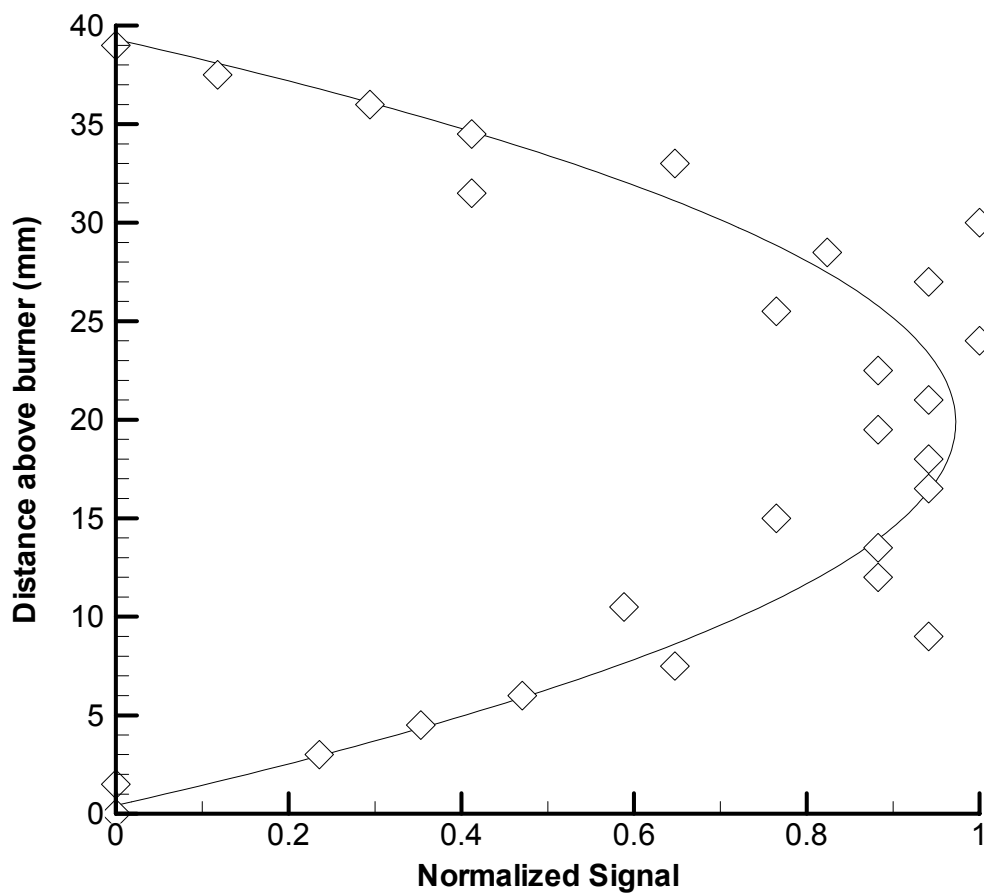


Figure 23: Energy distribution of laser sheet

4.2 Calibration Methodology

Utilizing the LII technique can always provide qualitative information such as that shown in the figures of § 4.1. Quantitative information, such as a soot volume fraction, is much more desirable and can be obtained if the LII image is calibrated to a known soot concentration. In the past, researchers have calibrated LII images by equating the average LII signal value of a specific region in an image to the average soot volume fraction measured in that same region with a different technique. The particular region of choice for determining a calibration factor was the region that produces the most soot, i.e., had the highest soot volume fraction. The disadvantage to this technique is that when LII signals are collected, the signal intensity is a “projected intensity.” A projected signal has been influenced by signal trapping and absorption of laser sheet energy; this is not the true for unattenuated LII signals. The signal trapping occurs because as the laser beam passes through a small cross-section of the flame and the detector is located perpendicular to the direction of the laser beam, the signal emitted from the heated soot particles must pass through the soot field that lies between the laser sheet and detector. Bryce et al. (2000) showed that when investigating the more heavily sooting regions of a flame, the attenuated signal could be as much as 18% less than the unattenuated signal. The signal is further corrupted by the fact that the soot particles exposed to the laser sheet are absorbing the energy of the laser sheet; as the laser passes through the flame, the energy of the laser sheet is continually decreasing. This phenomenon of laser sheet absorption or attenuation is evident in Figures 21b and 21c as the signal on the left side is much greater than that on the

right side and the direction of the laser propagation is left to right. Thus the calibration factor found using traditional calibration techniques is erroneous as it is based on a projected LII intensity. Shaddix and Smyth (1996) report that corrections for signal trapping and laser sheet attenuation are necessary in flames with soot loadings greater than 1 ppm. The flames studied in this work have soot loadings well above 1 ppm. A calibration methodology developed by Choi and Jensen (1998) accounts for both signal trapping and laser energy sheet losses. This methodology uses the unattenuated signal and yields a soot concentration calibration factor that is only influenced by the LII optical system and not by the amount of soot contained within the flame.

The methodology developed by Choi and Jensen (1998) and utilized with experimental data by DeCroix and Roberts (2000) will be discussed briefly. Figure 24 shows the top view of a typical axisymmetric diffusion flame that has been decomposed into J concentric circles. The center of the rings is positioned at the centerline of the flame. The rings are located at the midpoint of adjacent pixels, $\Delta x/2$, in the LII image; the last ring was located at the pixel corresponding to the edge of the flame. The laser sheet used for LII measurements would pass through the flame at $y=0$, perpendicular to the x - y plane, and in the direction of the x -axis. The attenuated intensity projected from the laser sheet location ($y=0$) to the camera detector is I_p . The $I_p(j)$ shown in Figure 24 is the projected LII intensity at $x=j$; it is the goal of the calibration methodology to correct this I_p to an unattenuated intensity, I . The value $y_{j,j+1}$ is the chordlength (beginning at the edge of the ring j and ending at the edge of ring $j+1$) that a projected signal $I_p(j)$ must pass through en

route to the camera detector. Each chordlength, $y_{j,j}$, is determined from trigonometry and is identical to a pathlength that would yield a soot volume fraction $f_{sv}(j)$.

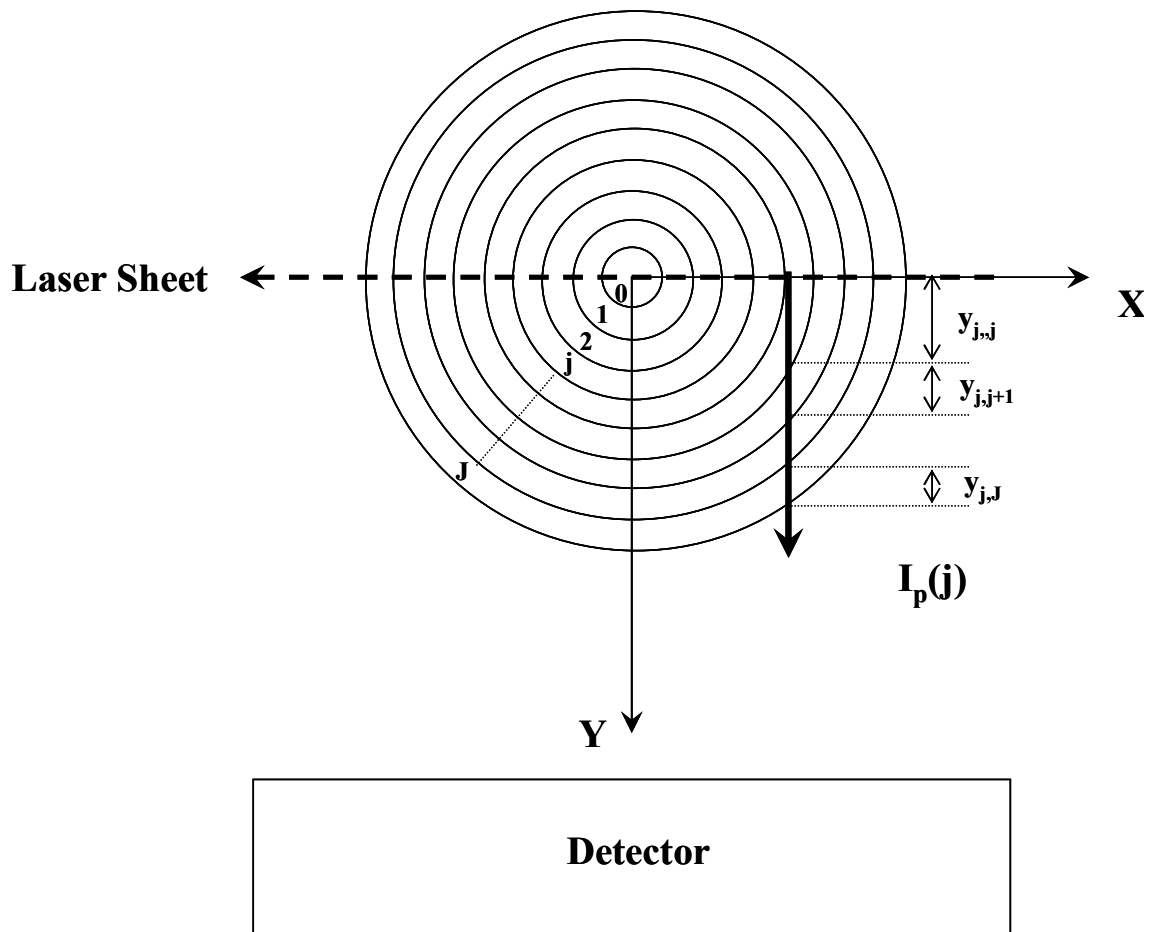


Figure 24: Decomposition of flame into J concentric rings (Choi & Jensen, 1998)

The following relationship relates the corrected intensity at pixel j along the centerline to the projected intensity observed by the detector:

$$I(j) = I_p(j) \exp \left[\frac{6\pi E(\tilde{m}) \left(\sum_{i=j}^J f_{sv}(j) \cdot y_{j,i} \right)}{\lambda} \right] \quad (4.1)$$

where λ is the detection wavelength and

$$E(\tilde{m}) = -\text{Im} \left[\frac{\tilde{m}^2 - 1}{\tilde{m}^2 + 2} \right] \quad (4.2)$$

where \tilde{m} is the index of refraction of soot and taken to be 1.57-i0.56 for reasons discussed in § 1.3.1. Since Choi and Jensen's calibration factor, CF, provides a relationship between I and f_{sv} , equation 4.1 can be rewritten as

$$I(j) = \frac{f_{sv}(j)}{CF} = I_p(j) \exp \left[\frac{6\pi E(\tilde{m}) \left(\sum_{i=j}^J f_{sv}(j) \cdot y_{j,i} \right)}{\lambda} \right] \quad (4.3)$$

The unknowns in equation 4.3 are $f_{sv}(j)$ and CF. If the value for CF is known, equation 4.3 can be iteratively solved at each pixel marching from $j=J-1$ to $j=0$. The collected LII signal at the outer edge of the flame can be assumed to be unattenuated since it does not pass through a soot field en route to the camera detector nor has the laser sheet been attenuated by any soot field within the flame; thus, $I(J)=I_p(J)$.

Initially, a guessed calibration factor was used to calculate the corrected soot volume fraction profile. Equation 4.4 was used to integrate this profile over the full pathlength of the flame to calculate a predicted transmission.

$$\left(\frac{I}{I_0}\right)_p = \exp\left[\frac{-6\pi E(\tilde{m})\left[\Delta x \cdot f_{sv}(0) + 2\Delta r \cdot \sum_{j=1}^{J-1} f_{sv}(j) + \Delta x \cdot f_{sv}(J)\right]}{\lambda}\right] \quad (4.4)$$

where Δx is the spacing between concentric rings. The predicted transmission was then compared to the experimental transmission found through laser light extinction measurements described in § 2.4. A new guess for the calibration factor was chosen and equations 4.3 and 4.4 were solved iteratively until a calibration factor was converged upon. DeCroix wrote a FORTRAN program that uses this iterative approach to find a calibration factor and corrected f_{sv} profile. The program was extensively tested with artificial soot volume fraction profiles; the methodology, source code and verification of the code are available in the dissertation of DeCroix (1998). The programs written by DeCroix were used to find the calibration factors and generate corrected images for the diffusion flames investigated in this work.

The calibration factor determined through this methodology should be applicable at every point in the flame. DeCroix and Roberts found that the calibration factors determined for the co-flow flames used in their work were nearly constant at flame heights between 25% and 80% of the total flame height. The axial location chosen for extinction measurements in this work was within that range. Additionally, the calibration factor should only be a function of a given experimental setup, which includes such parameters as pump intensity, camera gain, and camera quantum efficiency.

4.3 Calibration of LII Images

The intensity ratios given in Appendix 8.6 for the methane-air and ethylene-air flames at 65% of the flame height were used in the calibration code. The diameter of the HeNe laser beam used in the extinction measurements was measured to be about 300 μm , which is approximately the thickness of the laser sheet used in the LII measurements; this diameter corresponded to 5 pixel rows. These rows were averaged and used in the FORTRAN program `input.for` (DeCroix, 1998) to find the pixel locations of the start and end of the soot region and the centerline of the flame. A calibration factor of 0.005 ppm/count was found using the FORTRAN program `calib.for` (DeCroix, 1998); then, the flame images were simultaneously corrected for signal trapping and beam attenuation and calibrated to give quantitative information about the soot field. As noted in § 4.2, the calibration methodology requires axisymmetry of the flame. This requirement is a result of the calibration algorithm being performed on only the left half of the flame image. The left half of the flame image was used because the laser was entering the field of view from the left. The resulting half image was then rotated to give a complete image of the flame. Figure 25 shows both a raw and calibrated image. Note that in Figure 25a the flame is smoking; this smoking is not evident in Figure 25b because the left side of the flame was used in the correction and calibration algorithm. The smoke is drifting to the right side of the flame; thus, when the corrected and calibrated left side of the flame is rotated, the image of the smoke is lost.

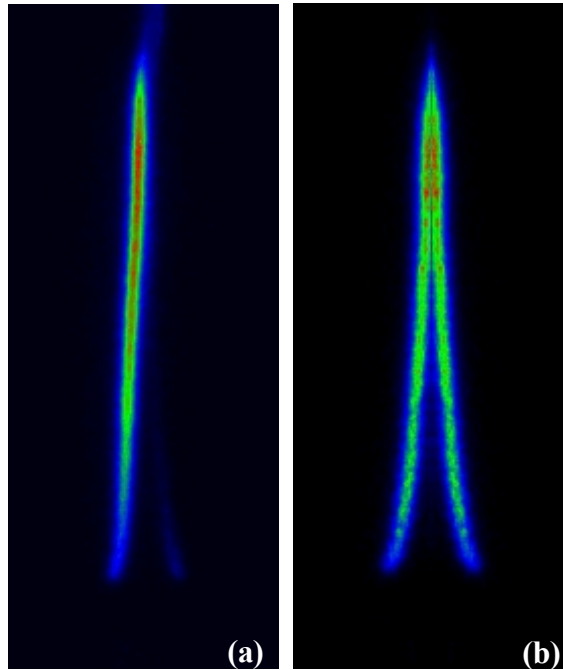


Figure 25: (a) Uncalibrated and uncorrected LII image and (b) calibrated and corrected LII image of ethylene-air flame at 16 atm

Figure 26Figure 34 show the measured f_{sv} in the flame at increasing pressures using methane and ethylene as fuels. In each of these images, the color scale representative of f_{sv} in parts per million (ppm) is not normalized, i.e., each image is scaled to its particular maximum f_{sv} . The influence of fuel type on soot yield is apparent in these images as the ethylene-air flame has a higher soot volume fraction than the methane-air flame at a given pressure.

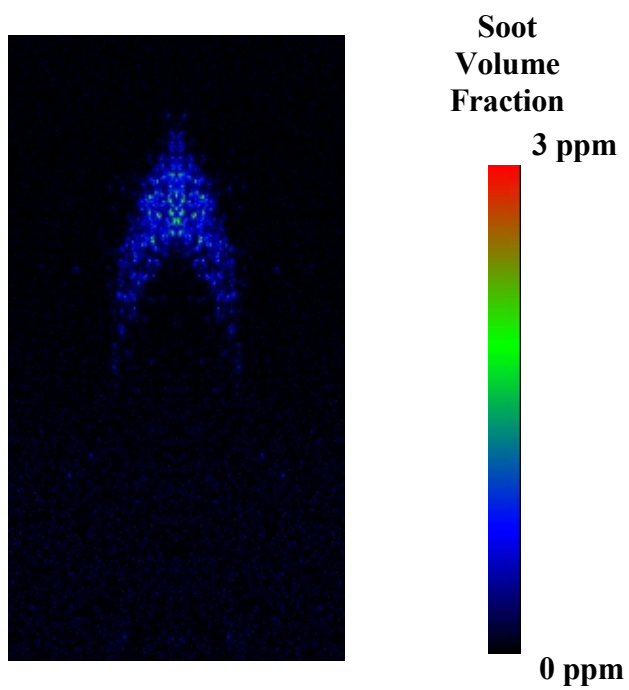


Figure 26: Soot volume fraction in methane-air flame at 2 atm

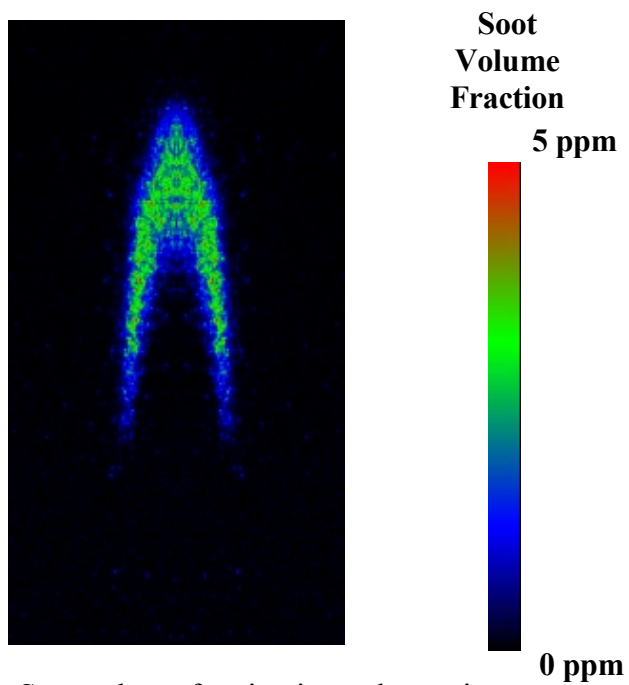


Figure 27: Soot volume fraction in methane-air flame at 4 atm

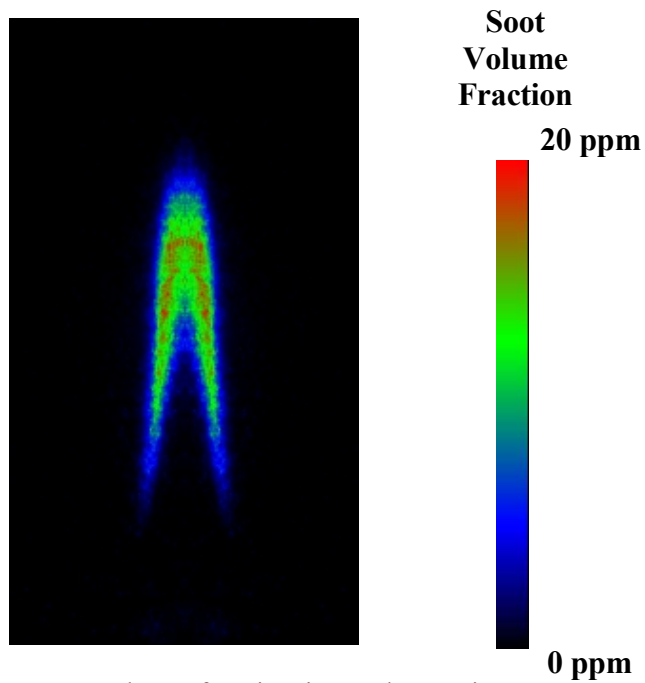


Figure 28: Soot volume fraction in methane-air flame at 8 atm

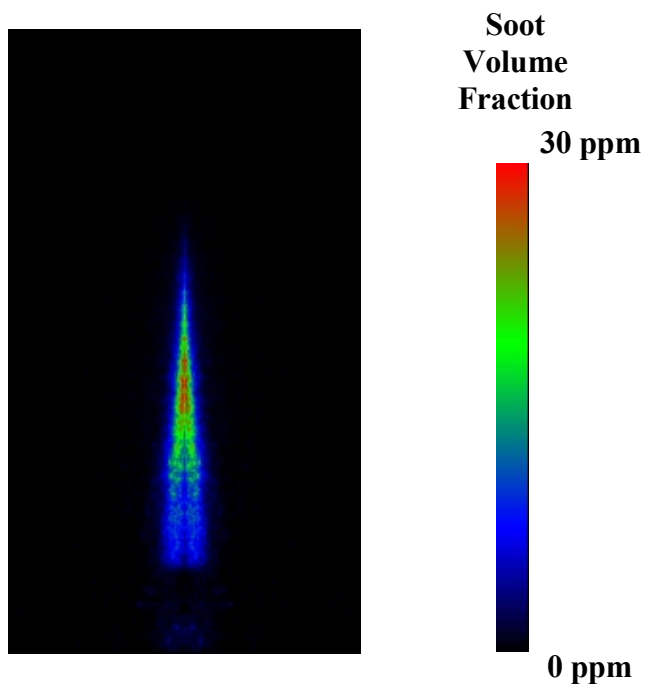


Figure 29: Soot volume fraction in methane-air flame at 16 atm

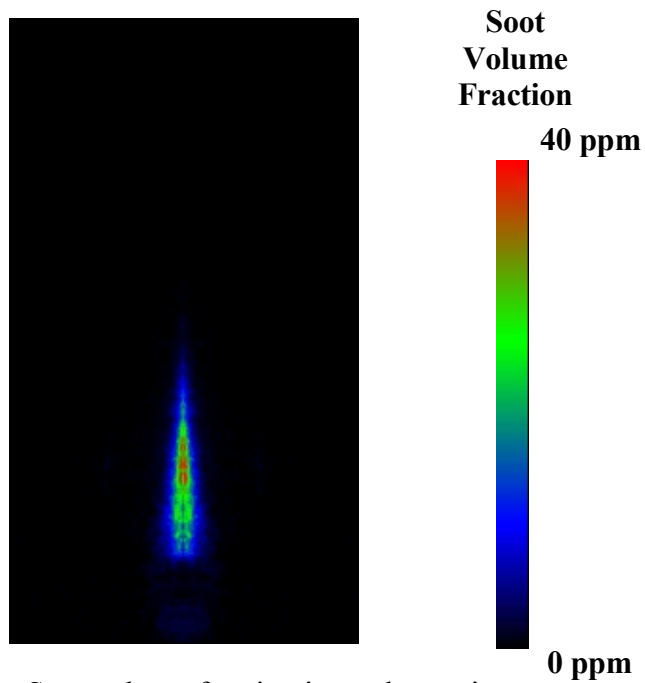


Figure 30: Soot volume fraction in methane-air flame at 25 atm

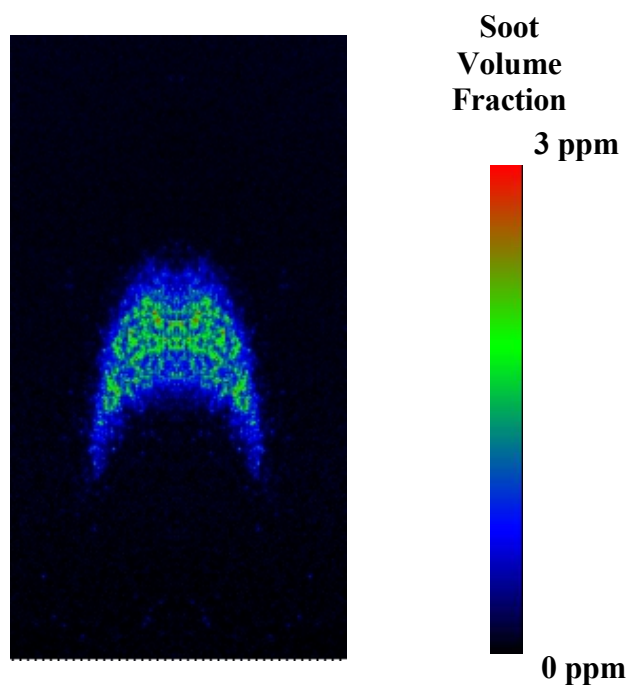


Figure 31: Soot volume fraction in ethylene-air flame at 1 atm

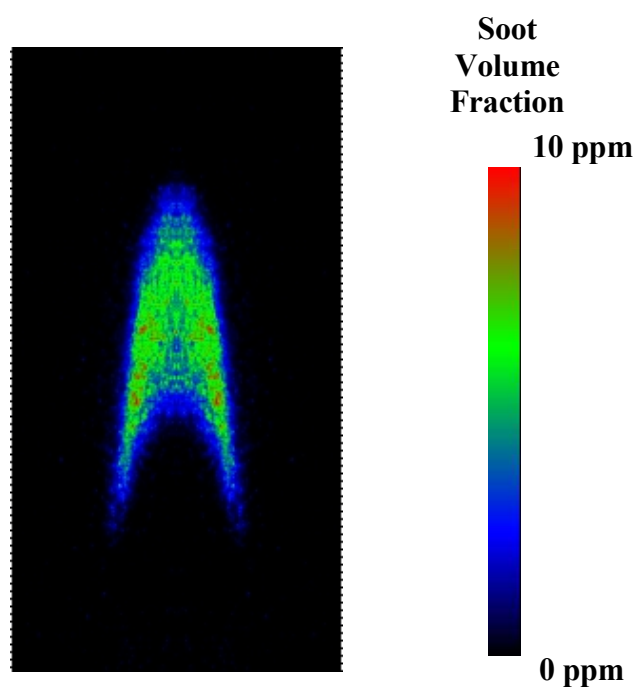


Figure 32: Soot volume fraction in ethylene-air flame at 2 atm

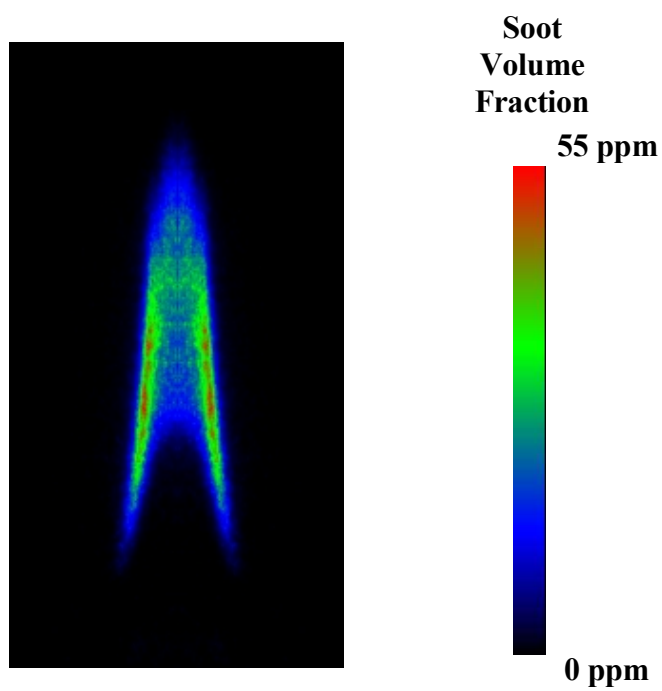


Figure 33: Soot volume fraction in ethylene-air flame at 4 atm

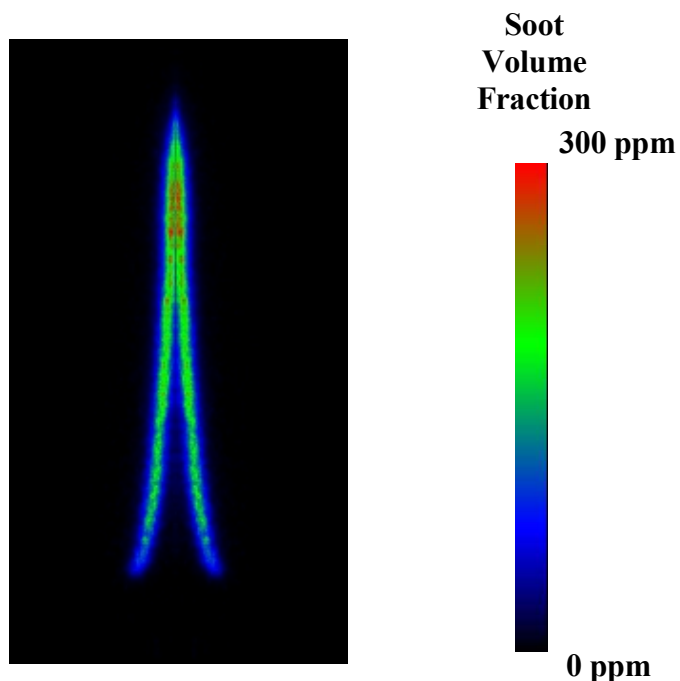


Figure 34: Soot volume fraction in ethylene-air flame at 16 atm

As pressure increases, the regions of high soot yield shift. This can be observed when comparing the methane-air flame at 8 atm (Figure 28) and 25 atm (Figure 30). At 8 atm, the peak sooting regions are located on the sides of the flame, and as the pressure increases to 25 atm, the tip of the flame becomes the highest sooting region. Figures 35 and 36 give more striking views of the effects of pressure on soot production and flame shape. These calibrated LII images have been normalized to the highest sooting case – 25 atm for the methane-air flame and 16 atm for the ethylene-air flame. When shown on the same scale as the highest pressure case, the soot field for the lowest pressure case is hardly distinguishable. These images also reiterate the physical changes the flame undergoes with increasing pressure, namely a significant narrowing of the flame.

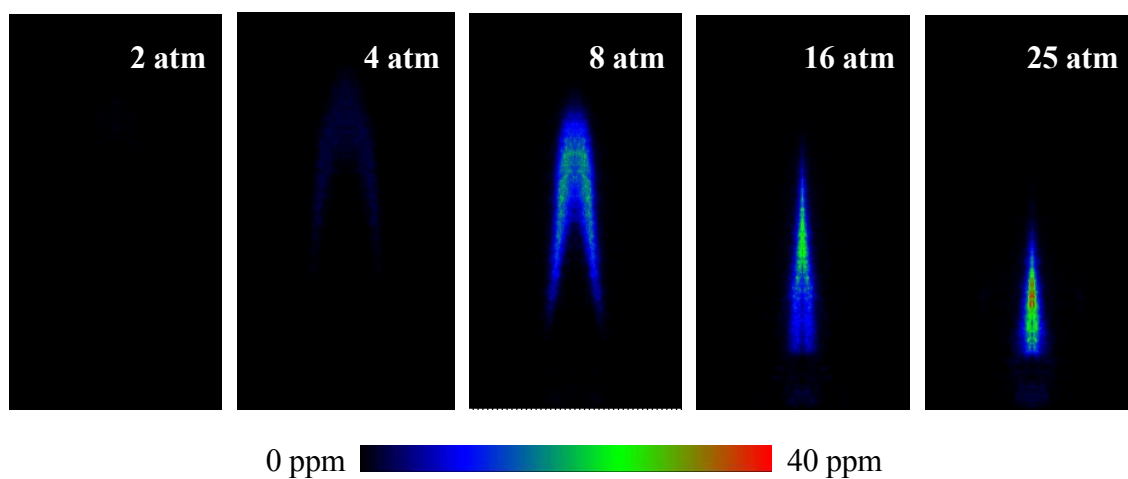


Figure 35: Calibrated and corrected LII images of methane-air flame normalized to maximum f_{sv} of 25 atm case

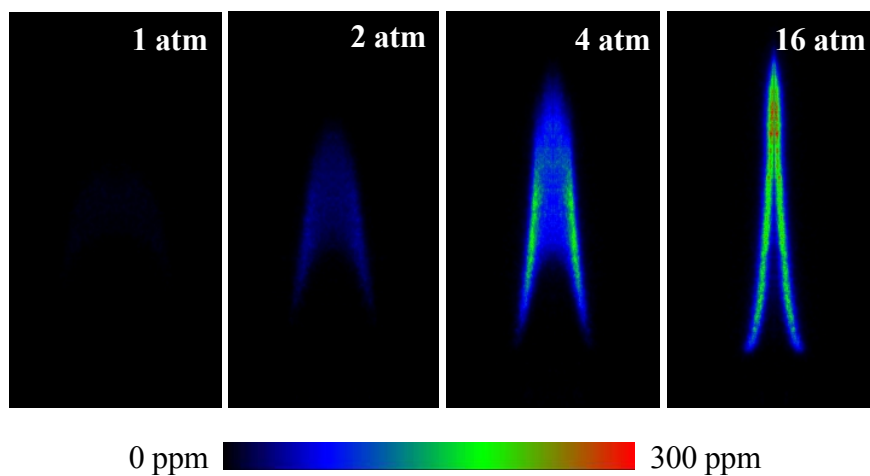


Figure 36: Calibrated and corrected LII images of ethylene-air flame normalized to maximum f_{sv} of 16 atm case

5 Conclusions

A better understanding of the formation of soot is desired in order to gain a more comprehensive picture of combustion processes and to reduce the resulting emission of soot particulates into the environment. Examining soot at elevated pressures is especially relevant as most work-producing devices operate at high pressures in order to gain thermodynamic efficiency. The present work has explored the formation of soot at elevated pressures up to 25 atm in a methane-air co-flow diffusion flame and up to 16 atm in an ethylene-air co-flow diffusion flame. The non-intrusive LII diagnostic technique was employed to gain spatially and temporally resolved measurements of the soot volume fraction. This research is unique in that it represents the first time that spatially and temporally resolved measurements of soot volume fraction in a diffusion flame have been taken at elevated pressures up to 25 atm. The conclusions obtained from this research are listed below.

Path Averaged f_{sv}

- 1.) The pressure dependences of the path averaged f_{sv} for the methane-air and ethylene-air flames are found to be $P^{0.65}$ and $P^{1.7}$, respectively.
- 2.) The path averaged f_{sv} for the ethylene-air flame compares well with published results. There are no previously published methane-air flame measurements of $f_{sv,ave}$ at elevated pressures.

Physical Characteristics of Flame

- 1.) Methane-air and ethylene-air flames are no longer optically thin above 8 atm and 2 atm, respectively, indicating that the path averaged f_{sv} measurements made above these pressures are questionable.
- 2.) Flame structure changes dramatically with increasing pressure. With velocity matched fuel and air flow rates that produce a flame with a height of 60 mm, the flame becomes very contorted and profoundly influenced by buoyancy-driven instabilities.
- 3.) A greatly over-ventilated flame is required for flame stability at elevated pressures. The fuel and air flow rates are not velocity matched in this case and a flame with an approximate height of 20 mm is used.
- 4.) The physical shape of the flame is very sensitive to increases in pressure. The flame becomes shorter in height and considerably narrower with increasing pressure. The path length of the methane-air flame scales with pressure as $p^{-0.46}$ and the path length of the ethylene-air flame as $p^{-0.57}$. The region of the flame responsible for precursor formation also becomes narrower.

Spatially and Temporally Resolved f_{sv}

- 1.) LII images of the soot field are corrected and calibrated to give spatially and temporally resolved, quantitative information about the soot field.

- 2.) Peak f_{sv} pressure dependence for the methane-air flame is $p^{1.2}$ and for the ethylene-air flame is $p^{1.7}$, which varies from the path averaged f_{sv} pressure dependence.
- 3.) The region of peak f_{sv} shifts from the wings of the flame to the tip with increasing pressure.

6 Future Work

The operation of the high pressure diffusion flame burner while conducting LII measurements was well documented in this work. Some changes in the operation of the burner, ranging in ease of implementation from relatively simple to very difficult, would provide even more worthwhile areas to investigate in the future. One simple change would be to add diluents to the fuel and thereby provide an opportunity to examine diffusion and transport issues. A second possibility would be to experiment with different fuel flow rates and pressures to verify the smoke point regions of the flame. A more difficult undertaking would be to modify the burner and pressure vessel such that they could be operated while descending in a drop tower. The moments of microgravity would allow soot formation at high pressures to be examined while buoyancy forces were eliminated.

7 References

- Axelsson, B., Collin, R., and Bengtsson, P., "Laser-induced incandescence for soot particle size measurements in premixed flat flames," *Appl. Opt.* **39**, 3683-3690 (2000).
- Axelsson, B., Collin, R., and Bengtsson, P. E., "Laser-induced incandescence for soot particle size and volume fraction measurements using on-line extinction calibration," *Appl. Phys. B* **72**, 367-372 (2001).
- Barfknecht, T. R., "Toxicology of soot," *Prog. Energy Combust. Sci.* **9**, 199-237 (1983).
- Bockhorn, H., Geitlinger, H., Jungfleisch, B., Lehre, Th., Schön, A., Streibel, Th., and Suntz, R., "Progress in characterization of soot formation by optical methods," *Phys. Chem. Chem. Phys.* **4**, 3780-3793 (2002).
- Bohren, C. F. and Huffman, D. R., *Absorption of Scattering of Light by Small Particles*, Wiley, 1983.
- Bryce, D. J., Ladommatos, N., and Zhao, H., "Quantitative investigation of soot distribution by laser-induced incandescence," *Appl. Opt.* **39**, 5012-5022 (2000).
- Burke, S. P. and Schumann, T. E. W., "Diffusion flames," *Proceedings of the First and Second Symposium on Combustion*, The Combustion Institute, 2-11 (c.1965).
- Choi, M. Y. and Jensen, K. A., "Calibration and correction of laser-induced incandescence for soot volume fraction measurements," *Combust. Flame* **112**, 485-491 (1998).
- Comstock, M. L., "Diesel exhaust in the occupational setting – Current understanding of pulmonary health effects," *Clinics in Lab. Med.* **18**, (1998).
- D'Alessio, A., Beretta, F., and Venitazzi, C. "Optical investigations on soot forming methane-oxygen flames," *Combust. Sci. Tech.* **5**, 263 (1972).

- Dalzell, W. H. and Sarofim, A. F., "Optical constants of soot and their application to heat-flux calculations," *J. Heat Transfer* **91**, 100 (1969).
- DeCroix, M. E., "The effects of unsteady hydrodynamics on soot formation in a counterflow diffusion flame," NC State University, Dissertation (1998).
- DeCroix, M. E. and Roberts, W. L., "Transient flow field effects on soot volume fraction in diffusion flames," *Combust. Sci. Tech.* **160**, 165-189 (2000).
- Eckbreth, A. C., "Effects of laser-modulated particulate incandescence on Raman scattering diagnostics," *J. Appl. Phys.* **48**, 4473-4479 (1977).
- Fischer, B. A. and Moss, J. B., "The influence of pressure on soot production and radiation in turbulent kerosine spray flames," *Combust. Sci. and Tech.* **138**, 43-61 (1998).
- Flower, W. L. and Bowman, C. T., "Measurements of the effect of elevated pressure on soot formation in laminar diffusion flames," *Combust. Sci. and Tech.* **37**, 93-97 (1984).
- Flower, W. L. and C. T. Bowman, "Soot production in axisymmetric laminar diffusion flames at pressures from one to ten atmospheres," Twenty-first Symposium (International) on Combustion, The Combustion Institute, 1115-1124 (1986).
- Flower, W. L., "The effect of elevated pressure on the rate of soot production in laminar diffusion flames," *Combust. Sci. and Tech.* **48**, 31-43 (1986).
- Flower, W. L., "Observations on the soot formation mechanism in laminar ethylene-air diffusion flames at one and two atmospheres," *Combust. Sci. and Tech.* **53**, 217-224 (1987).
- Frenklach, M., "Reaction mechanisms of soot formation in flames," *Phys. Chem. Chem. Phys.* **4**, 2028-2037 (2002).
- Gaydon, A. G. and Wolfhard, H. G., *Flames: their structure, radiation and temperature*, 3rd ed., Chapman & Hall: London, 1970.

- Glassman, I., *Combustion*, 2nd ed., Harcourt Brace Jovanovich: New York, 1987.
- Heidermann, T., Jander, H., and Wagner, H. G., "Soot particles in premixed C₂H₄-air flames at high pressures (P=30-70 bar)," *Phys. Chem. Chem. Phys.* **1**, 3497-3502 (1999).
- Hu, D., Braun-Unkloff, M., and Frank, P., "Modeling study on initial soot formation at high pressures," *Zeitschrift für Physikalische Chemie* **214**, 473-491 (2000).
- Jost, Wilhelm, trans. by Huber Croft, *Explosion and Combustion Processes in Gases*, 1st ed., McGraw-Hill: New York, 1946.
- Kadota, T., Hiroyasu, H., and Farazandehmer, A., "Soot formation by combustion of a fuel droplet in high pressure gaseous environments," *Combust. Flame* **29**, 67 (1977).
- Kazakov, A., Wang, H., and Frenklach, M., "Detailed modeling of soot formation in laminar premixed ethylene flames at a pressure of 10 bar," *Combust. Flame* **100**, 111-120 (1995).
- Li, Y., "Applications of Transient Grating Spectroscopy to Temperature and Transport Properties Measurements in High-Pressure Environments," NC State University, Dissertation (2001).
- McArragher, J. S. and Tan, K. J., "Soot formation at high pressure: a literature review," *Combust. Sci. Tech.* **5**, 257 (1972).
- Melton, L. A., "Soot diagnostics based on laser heating," *Appl. Opt.* **23**, 2201-2208 (1984).
- Millberg, M. E., "Carbon formation in an acetylene-air diffusion flame," *J. Phys. Chem.* **63**, 578 (1959).
- Miller, I. M. and Maahs, H. G., "High-pressure flame system for pollution studies with results for methane-air diffusion flames," NASA TN D-8407 (1977).

- Miller, I. M. and Maahs, H. G., "Effect of pressure on structure and NO_x formation in CO-air diffusion flames," NASA TN D-1448 (1979).
- Miller, I. M. and Maahs, H. G., "Pollutant emissions from flat-flame burners at high pressures," NASA TN D-1673 (1980).
- Morgan, W. K. C., Reger, R. B., and Tucker, D. M., "Health effects of diesel emissions," *Ann. Occup. Hyg.* **41**, 643-658 (1997).
- Palmer, H. B. and Cullis, H. F., *The Chemistry and Physics of Carbon*, vol. 1, Marcel Dekker: New York, 1965.
- Parker, W. G. and Wolfhard, H. G., "Carbon formation in flames," *J. Chem. Soc.*, 2038-2049 (1950).
- Quay, R., Lee, T., Ni, T., and Santoro, R. J., "Spatially resolved measurements of soot volume fraction using laser-induced incandescence," *Combust. Flame* **97**, 384-392 (1994).
- Richter, H. and Howard, J. B., "Formation of polycyclic aromatic hydrocarbons and their growth to soot – a review of chemical reaction pathways," *Prog. Energy Combust. Sci.* **26**, 565-608 (2000).
- Santoro, R. J. and Shaddix, C. R., "Laser-induced incandescence," *Applied Combustion Diagnostics*. Taylor & Francis: New York, 2002.
- Schalla, R. L. and McDonald, G. E., "Mechanisms of soot formation in diffusion flames," Fifth Symposium (International) on Combustion, The Combustion Institute, Pittsburgh, 316 (1955).
- Scheepers, P. T. J. and Bos, R. P., "Combustion of diesel fuel from a toxicological perspective 2. toxicity," *Int. Arch. Occup. Environ. Health* **64**, 163-177 (1992).

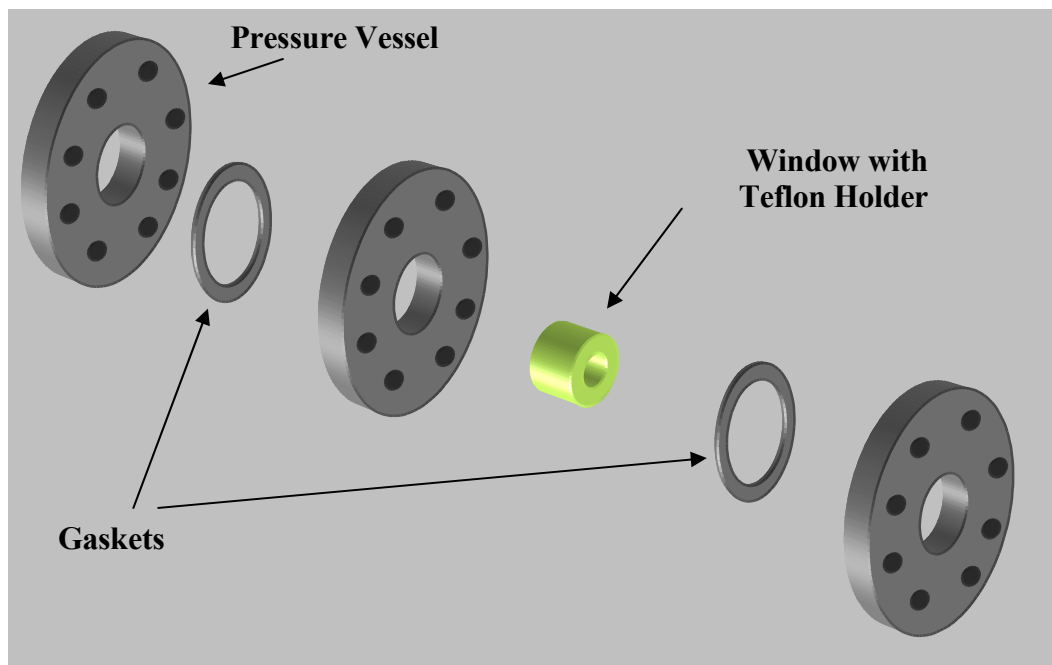
- Schittkowski, T., Mewes, B., and Bruggemann, D., "Laser-induced incandescence and Raman measurements in sooting methane and ethylene flames," *Phys. Chem. Chem. Phys.* **4**, 2063-2071 (2002).
- Shaddix, C. R. and Smyth, K. C., "Laser-induced incandescence measurements of soot production in steady and flickering methane, propane, and ethylene diffusion flames," *Combust. Flame* **107**, 418-452 (1996).
- Starke, R. and Roth, P., "Soot particle sizing by LII during shock tube pyrolysis of C₆H₆," *Combust. Flame* **127**, 2278-2285 (2002).
- Sydbom, A., Blomberg, A., Parnia, S., Stenfors, N., Sandstrom, T., and Dahlen, S. E., "Health effects of diesel exhaust emissions," *European Respiratory J.* **17**, 733-746 (2001).
- Van de Hulst, H. C., *Light Scattering by Small Particles*, Dover: New York, 1957.
- Vander Wal, R. L. and Weiland, K. J., "Laser-induced incandescence: Development and characterization towards a measurement of soot-volume fraction," *Appl. Phys. B* **59**, 445-452 (1994).
- Vander Wal, R. L., Choi, M. Y., and Lee, K., "The effects of rapid heating of soot: Implications when using laser-induced incandescence for soot diagnostics," *Combust. Flame* **102**, 200-204 (1995).
- Vander Wal, R. L., Zhou, Z., and Choi, M. Y., "Laser-induced incandescence calibration via gravimetric sampling," *Combust. Flame* **105**, 462-470 (1996).
- Vander Wal, R. L., "Laser-induced incandescence: detection issues," *Appl. Opt.* **35**, 6548-6559 (1996).
- Vander Wal, R. L. and Jensen, K. A., "Laser-induced incandescence: excitation intensity," *Appl. Opt.* **37**, 1607-1616 (1998).

- Vander Wal, R. L. and Ticich, T. M., "Cavity ringdown and laser-induced incandescence measurements of soot," *Appl. Opt.* **38**, 1444-1451 (1999).
- Vander Wal, R. L., Ticich, T. M., and Stephens, A. B., "Can soot primary particle size be determined using laser-induced incandescence?" *Combust. Flame* **116**, 291-296 (1999).
- Wagner, H. G., Seventeenth Symposium (International) on Combustion, The Combustion Institute, Pittsburgh, 3 (1979).
- Wagner, H. G., ed. by D. Siegl & G. Smith, "Soot formation – an overview," *Particulate Carbon: Formation During Combustion*, Plenum: New York, 1981.
- Welle, E., "The frequency response of counterflow diffusion flames," NC State University, Dissertation (2002).
- Will, S., Schraml, S., and Leipertz, A., "Two-dimensional soot-particle sizing by time-resolved laser-induced incandescence," *Opt. Lett.* **20**, 2342-2344 (1995).
- Zhang, Z. and Ezekoye, O. A., "Soot production rate calculations at elevated pressure in a methane-air jet diffusion flame," *Combust. Sci. and Tech.* **137**, 323-346 (1998).

8 Appendices

8.1 Pressure Vessel Window Assembly

The pressure vessel windows should be cleaned with alcohol. Prior to reinstalling the cleaned windows, a thin layer of vacuum grease should be applied to the circumference of the window and the inside surfaces of the window's Teflon holder. The window should then be carefully pressed into the Teflon holder. The Teflon holder is then inserted into the middle flange as shown below.



8.2 Pressure Build-up Methodology

The exhaust flow of the high pressure vessel is controlled by a needle valve. Approximately five and one half turns fully closes the valve. While trying to maintain a flame within the pressure vessel, it is imperative that the needle valve never be fully closed as the flame will without exception extinguish. The following two tables show the methodologies for maintaining a methane-air flame up to a pressure of 25 atm and an ethylene-air flame up to a pressure of 16 atm.

Pressure (atm)	Methane (slpm)	Co-flow Air (slpm)	Window Port Air (slpm)	Total Downward Turns of Needle Valve
1	0.10	20.0	10.0	0.00
2	0.10	20.0	25.5	3.50
4	0.10	20.0	40.0	4.50
8	0.10	20.0	85.0	4.75
16	0.15	30.0	110.0	5.00
25	0.15	30.0	110.0	5.10

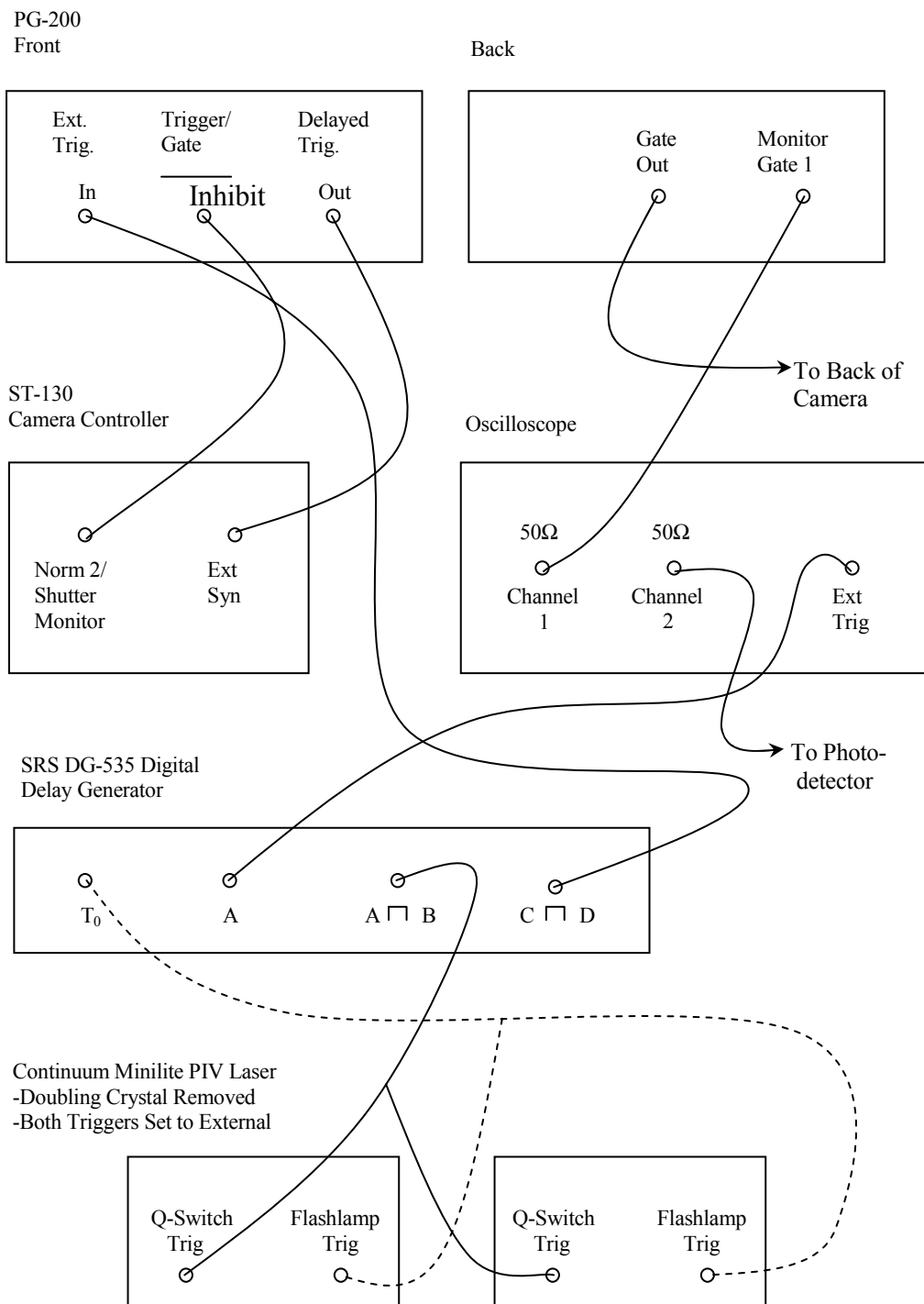
Pressure (atm)	Ethylene (slpm)	Co-flow Air (slpm)	Window Port Air (slpm)	Total Downward Turns of Needle Valve
1	0.06	20.5	10.0	0.00
2	0.06	20.5	30.0	3.50
4	0.06	20.5	45.0	4.75
8	0.06	20.5	85.0	5.00
16	0.06	20.5	110.0	5.25

8.3 LII Measurements: Operating Procedure

- 1.) Turn on Hastings Model 40 Power Supply for the flow meters and allow to warm up for one hour.
- 2.) Turn on N₂ to camera. Wait 15 minutes.
- 3.) Turn on water to camera and pressure vessel. Wait 10 minutes
- 4.) Turn on detector controller (two switches). Wait 10 minutes after green light has come on.
- 5.) Meanwhile, set flow rates for fuel and air.
- 6.) Turn on PG-200, Signal Delay Generator DG 535, Oscilloscope, Photodetector, Laser and computer.
- 7.) Take flat field images with camera lens capped.
- 8.) Remove camera lens cover and attach filter (mirror-like side facing away from the flame).
- 9.) Remove plastic coverings from optics.
- 10.) Open both exhaust needle valve and two-way valve fully. (Burner will not ignite with two-way valve closed.)
- 11.) Light Burner. (Turn on fuel to burner. Immediately light burner. Turn on air to burner. Turn on air to window ports.)
- 12.) Turn on exhaust fan.
- 13.) Slowly close two-way valve.
- 14.) Turn on laser with appropriate beam dump in place.
- 15.) Collect images using IPLab software.

When finished collecting data, turn fuel off at bottle and allow excess fuel in fuel line to burn away. Then turn off air supplies and equipment. Turn off water to camera and allow the N₂ to flow for 10-15 minutes before turning off as well. Cover optics and turn off exhaust fan.

8.4 LII Wiring Schematic



8.5 IPLab Settings

Press F1 to view Camera Setup. Options selected are listed below:

From: One Camera

Mode: Synchronous

10 Frames

Exposure: 0 sec

Timing Mode: Ext Syn

Number of Cleans: 1 and Continuous Cleans is selected

Shutter Control: Open Before Signal is selected

8.6 Average Extinction Data

Methane - 85% Flame Height

p(atm)	I / I ₀	L (m)	f _{sv} (ppm)
2	0.871	0.00304	5.95
4	0.832	0.00235	10.13
6	0.745	0.00189	20.14
8	0.717	0.00160	26.96
10	0.730	0.00123	33.02

Methane - 65% Flame Height

p(atm)	I / I ₀	L (m)	f _{sv} (ppm)
1	0.904	0.00470	2.771
2	0.912	0.00408	2.928
4	0.902	0.00278	4.818
6	0.914	0.00230	5.054
8	0.875	0.00190	9.118
10	0.747	0.00167	22.572

Ethylene - 65% Flame Height

p(atm)	I / I ₀	L (m)	f _{sv} (ppm)
1	0.883	0.00441	3.666
2	0.813	0.00321	8.355
4	0.530	0.00204	40.308
6	0.308	0.00174	88.018
8	0.256	0.00138	127.675
10	0.231	0.00116	163.386